UNIVERSITÀ DEGLI STUDI DI TRIESTE

UNIVERSITÀ DEGLI STUDI DI TRIESTE

XXXVI CICLO DEL DOTTORATO DI RICERCA IN

Earth Science, Fluid-Dynamics, and Mathematics. Interaction and Methods

ACOUSTIC CHARACTERIZATION OF AIR-BUBBLE FILMS IN A TURBULENT BOUNDARY LAYER

Settore scientifico-disciplinare: ICAR/01

DOTTORANDA
Naira Hamid

COORDINATORE PROF
Prof. Stefano Maset

SUPERVISORE DI TESI
Prof. Vincenzo Armenio

CO-SUPERVISORE DI TESI
Prof. Marta Cianferra

CO-SUPERVISORE DI TESI
Dr. Giovanni Petris

ANNO ACCADEMICO 2022/2023

Abstract

The scientific community has recently become more aware of noise pollution in the marine ecosystem. Human activities at sea generate impulsive and continuous noise sources that endanger the survival of marine species. Ongoing research and development focus on innovative mitigation devices and techniques. Among them, the bubble curtains represent air bubble barriers able to mitigate the level of crossing sound waves. This technique is currently adopted to reduce the impact of impulsive signals associated to off-shore construction or maintenance, thus helping to protect the surrounding ecosystems. Less attention has been given to the use of air bubble barriers to reduce continuous noise from sources such as propellers, which are responsible for 85% of the noise emitted by ships.

The numerical research presented in this thesis aims to examine the absorption of low-to-intermediate frequency underwater noise in air-water mixtures. The study focuses on a scenario where an immersed flat plate is covered by an air film, serving as a sound barrier. This setup is a representative model of a bubble injection system used to encase a part of a ship's hull, aiming to acoustically isolate a structure below the waterline. The study combines eddy-resolving fluid dynamics techniques to solve the complex inhomogeneous fluid flow and the solution of the wave equation in the time-space domain to characterize the properties of the air barriers when subjected to continuous noise sources.

The first part of this thesis focuses on conducting numerical experiments to simulate the fluid dynamics of a channel flow with a uniform air jet entering the domain. Turbulent flows are reproduced using Large Eddy Simulation (LES) at both low Reynolds number (LRN) ($Re_\tau = 180$) and high Reynolds number (HRN) ($Re_\tau = 8000$) scenarios, the second one considering a wall-model approach. The two-phase flow solution is determined using the volume of fluid (VoF) method. The primary goal of this initial part is to accurately calculate the distribution of density and speed of sound, which are essential for evaluating the properties of the acoustic environment and set the domain for the propagation of the acoustic source.

In the second part of the thesis, the propagation of acoustic waves incident to the air-water mixture layer is analyzed, by solving the acoustic wave equation in the three-dimensional physical (space-time) domain. Once the air-water mixture

layer is fully developed across the length of the channel, its sound absorbing capacity is investigated considering monochromatic monopole source. The noise signature is recorded at a probe positioned on the upper wall (characterized as a perfectly reflecting surface) to assess the noise reduction property of the air layer covering the plane.

The investigation focuses on the difference in the transmission of acoustic pressure between the pure water case and the air-water mixture layer case, both considering a mean distribution and an instantaneous distribution of the air layer. Thus, the effectiveness of the layer is analyzed with respect to the source's frequency and the air layer's distribution in space. The results show that the air film significantly reduces the acoustic signal incident to the plate, mostly for intermediate frequencies and when an average distribution of the mixture is considered. In particular, the averaged distribution of the air content within the layer largely increases the reduction of acoustic pressure incident to the plate compared to the instantaneous distribution of the flow field. The latter presenting a non-uniform distribution of the air along the upper wall. Additionally, as expected, the reduction in signal was notably enhanced, increasing the air layer's thickness.

Air bubble barriers are also utilized to minimize the destruction caused by cavitation erosion to water-submerged structures. Hence, the final part of the thesis is devoted to a preliminary numerical investigations concerning the dynamics of single cavitation bubble collapse close to the rigid surface. This study is crucial to understand the noise emission caused by bubble collapse and the erosion of the surface that can result from high velocities, pressures, and temperatures. The thermodynamical effects also play a significant role in the last stage of the bubble collapse. For this reason, temperature, pressure, and velocity field evolution over time during the process of collapsing is investigated. The pure vapor bubble model is employed, and its dynamics are assumed to be driven by inertia and compressible effects. The CompressibleInterFoam solver in OpenFoam is utilized by considering the mixture model and applying the VoF model. It is observed that during the collapse, the bubble exhibited high speed in the proximity of the wall. Moreover, the bubble contracted rapidly in the collapse stage, consequently exerting pressure on the vapor inside, leading to a significant temperature rise.

Contents

List of Figures

Chapter 1

Introduction

"The fact is that no species has ever had such wholesale control over everything on earth, living or dead, as we now have. That lays upon us, whether we like it or not, an awesome responsibility. In our hands now lies not only our own future but that of all other living creatures with whom we share the earth".

-David Frederick Attenborough

1.1 Background

The ocean fauna is endangered by underwater radiated noise (URN) produced by human activities. Anthropogenic activities that take place at sea, such as shipping (propeller cavitation and engine noise), construction (pile driving and dredging), seismic surveys or military activities (sonar and explosions), and offshore energy production (oil and gas extraction, tidal and wind turbines), contribute to the overall noise pollution of the marine environment [1].

Various noise reduction techniques have been investigated to minimize the impact of both continuous sources (reduction of vessel speed [2], implementation of ship-quieting technologies [3]) and impulsive sources (considering alternatives to airguns [4] or air-bubble barriers for piling operations). Nowadays, air-bubble barriers are widely employed to mitigate impulsive sound waves resulting from maritime industrial activities related to off-shore structures construction or maintenance [5, 6]. In particular, it has been shown that placing an air-bubble curtain during piling operations can help to reduce noise [7, 8, 9, 10]. Other engineering applications advocate for the injection of an air-bubble layer both to reduce drag [11, 12, 13] and to lessen cavitation erosion on underwater structures [14, 15]. Efforts to reduce underwater noise can be achieved by the emerging method called "air lubrication," in which the conventional water lubrication system beneath ships' hulls is replaced with air bubbles. The air between the hull and the water acts as a cushion to reduce the

drag that is caused by friction between the two. This, in turn, reduces vibrations and the noise generated from the nearby propeller, resulting in less underwater noise. For example, the Prairie/Masker Air System [16], developed by the US Navy post-World War II. This system used air bubbles covering the hull to mask engine noise or released bubbles around the propeller, aiming to make ships less detectable by sonar.

The physical properties of the medium (density and speed of sounds) determine the propagation of the acoustic waves and the amount of sound energy transmitted or reflected at an interface between two media. In an air-water mixture, the layers are often not separated by a well-defined interface, but rather, the mixed media is characterized by a continuous variation due to the interaction between the two phases. However, most of the research has been conducted on layered media [17], where an in-depth description of the theory of spherical acoustic waves incident to layered medium is described. It is worth mentioning that the application of ray theory for spherical and cylindrical waves may have limitations, which arise from the positioning of the source or radiator. For instance, when the distance between the source/radiator and the receiver is smaller or comparable to the wavelength, the diffraction effects are strongest, and ray theory becomes inapplicable.

Research on sound transmission through air-water interfaces has primarily focused on the transmission of sound waves from air to marine environments. Compared to theoretical and experimental studies, little attention has been paid to the propagation of acoustic waves in the air generated by immersed sources. Among others, [18, 19] showed that the non-homogeneous medium can significantly affect both the wavefront shape and amplitude depending on the location of the source. Contrary to common beliefs, the author demonstrated that the water-air interface does not always behave like a perfect mirror, finding an abnormal increase in the amount of energy transmitted from water to air; in particular, the water-air interface is anomalously transparent for low-frequency sound radiated in shallow waters [20, 21, 22]. Later, McDonald and Calvo [23, 24] confirmed experimentally this behavior when a low-frequency sound was generated near the interface within a fraction of the sound wavelength and defined it as the enhanced transmission of power in the air. Several experiments have been carried out simultaneously to confirm this phenomenon for a frequency range between 1 kHz to 20 kHz [25, 26, 27]. Ghadimi [28] also validated the experimental results using a numerical approach to study the frequency transmission in the range 2 kHz to 20 kHz sound through a smooth air-water interface for localized underwater shallow depth source. However, results obtained in laboratory studies are not comprehensive since they are focused on a very high-frequency range, which is not typical of realistic underwater noise sources.

Specific to bubbly flows, we mention the studies on the reflection and refraction of

acoustic waves at the interface between pure water and bubbly water, which were analyzed by Shagapov et al. [29]. They aimed to identify the critical incidence angles that allow for total wave reflection from the interface. Gubaidullin et al. [30, 31] analyzed the reflection coefficients of bubbles in a multilayered media with different bubble distributions. In a recent experimental study on acoustic wave reflection from a water layer with air bubbles conducted by Wang et al. [32], a correlation was found between the gas content in the water and the dependence of the reflection coefficient on perturbation frequency.

It is vital to understand the acoustic traits of gas-liquid mediums to investigate the propagation of sound waves in layered media containing bubbly liquid. Mallock [33], in 1910, was the first to apply mixture theory to "frothy liquids." He assumed that the bubbles in a liquid have the same speed of sound as homogeneous media of similar density and elastic properties. Wood [34] confirmed his work and introduced an equation widely used for the low-frequency sound speed in bubbly liquids that depends on the gas volume fraction, the compressibility, and the density of the gas and liquid. [35] further developed a theoretical framework for sound transmission in liquid-containing bubbles by including the effect of heat conduction. In 1989, Commander and Prosperetti [36] and Ruggles et al. [37] studied the sound propagation in bubbly liquids, specifically addressing energy dissipation and showed that the sound attenuation depends on the void fraction and the bubble size distribution. Later, Wilson [38, 39] conducted a comparison of theoretical models developed by [36, 37] and also verified experimentally the Wood's expression that relates the sound speed of a bubbly liquid to its void fraction.

Hence, various factors must be considered to model the air/bubble curtain and make it more effective. These include the size and distribution of the bubbles, the depth at which the air curtain is placed, and the frequency of the source/noise to be mitigated.

1.2 Objective

Despite the studies dedicated to understanding acoustic behavior in the case of bubbly-liquid media, the acoustic absorption in the air-water mixture layer still requires attention. The current study is motivated by the lack of numerical research on the sound absorption property of air films, as well as a mixture of air-water films, in case of underwater low-frequency noise, ranging from 1 Hz to 1000 Hz.

In our case, we do not consider a smooth interface but rather a mixture of non-condensable air and water. We obtain the non-homogeneous domain through a numerical simulation, considering a water turbulent channel flow and injecting a

thin layer of air next to the top boundary. Once the distribution of the air-water mixture is fully developed, covering the whole top boundary, a monopole source is used as a tonal source propagating in the mixture. The propagation of the acoustic waves incident on the mixture layer, representing a bubbly flow screen covering the upper plate of the channel, is evaluated by solving the acoustic wave equation in the three-dimensional space-time domain. The difference in the transmission of acoustic pressure between the pure water case and the mixture case is examined.

1.3 Methodology

An acoustic wave undergoes refraction and reflection when propagating in a heterogeneous medium characterized by gradients of density and speed of sound. The presence of an air-bubble layer can dramatically reduce the speed of sound, inducing a pronounced slowing down of the incident wave. We consider an air film covering a flat plate immersed in water, acting as a sound barrier. Among the possible technological applications, this archetypal model represents a bubble injection system adopted to wrap a part of the ship's hull. An accurate full-scale experiment should require the proper disposition of the holes along the hull, and, according to the flow rate of the air, the domain should be long enough to allow the adherence of the air film to the solid surface. In our numerical simulation, we reproduce a small region, assuming the plate to be flat. At the same time, the air film is obtained considering a homogeneous jet at the inlet of the domain (see Figure 1.1). In this way, we are able to study the local acoustic absorption downstream of the holes when the air film has already been reattached to the hull.

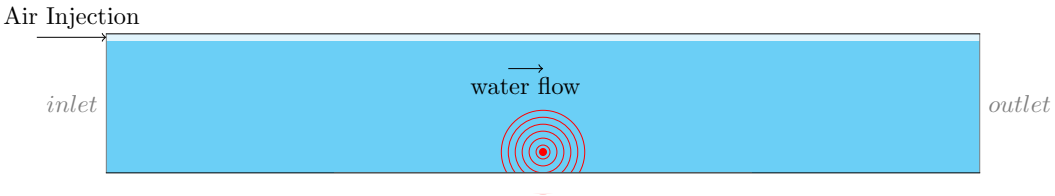

Figure 1.1: Schematic of the numerical experiment carried out for the evaluation of the noise absorption property of an air-bubble layer.

The mathematical modeling system is composed of two main steps. We first consider a fluid dynamic simulation of the air-water mixture, which allows us to obtain an accurate distribution of the gaseous phase within the carrying liquid. Then, the density and speed of sound distribution over the domain are extracted and adopted as input parameters for the acoustic propagation model. The propagation model

solves the acoustic wave equation using a Finite Difference Time Domain (FDTD) method, which is second-order accurate both in time and space. In this research, the acoustic source has been implemented using the hard and soft source injection method (see [40] for details on the implementation and relevant literature).

The preliminary tests conducted using this model initially considered simplified conditions with an air/water interface. An arbitrary thickness λ_{air} is assigned to the air layer, and the effectiveness of this air layer (compared to the homogeneous case) is studied as the wavelength of the signal varies. The two-phase channel was developed using the interFOAM solver, which numerically reproduces the dynamics of the air film at the flat plate. The final test represents the air barrier/curtain device, in which the real dimensions of parameters and air layer thickness are used.

The thesis is structured as follows: Chapter 2 discusses the dynamics of two-phase flows in which the mathematical model we used for our numerical experiment is reported. Chapter 3 discusses the implementation of turbulent numerical simulations in detail. Chapter 4 reports the propagation model implementation and test case of utilizing the model. Chapters 5 and 6 analyze the result of each case presented in detail and report the description of the case study, namely the acoustic Propagation in an air-water mixture layer simulated at low Reynolds number (LRN) and at high Reynolds number (HRN). Chapter 7 introduces a single cavitation bubble dynamics, which incorporates a bubble's temperature, pressure, and velocity effect near a wall. Chapter 8 provides the conclusion and recommendations for future work.

Chapter 2

Dynamics of two phase flows

In this chapter, a brief description of the characteristics, modeling, and numerical approaches of two-phase flow are mentioned. The section 2.2 describes the fluid-dynamic equations governing a two-phase flow and the derivation of the speed of sound in such dispersed homogeneous flow. Moreover, the numerical approaches for two-phase flows are discussed in section 2.3. In section 2.3.1, the mixture model with a volume fraction approach is presented that we utilize in this work for the simulation. In 2.4, the techniques to simulate the fluid flow are provided that will be used in this work

2.1 Types of two-phase flows

Any given element on Earth exists in one of three states: solid, liquid, or gas. The specific state of an element can impact both natural phenomena and human activities. A phase thermodynamically describes a distinct region of space occupied by a specific material in a defined state. In fluid dynamics, any flow involving more than one phase or component is defined as a multiphase flow. Moreover, the flows have some degree of phase/component separation in the continuum limit at a level well beyond the molecular scale.[41]. The simplest form of multiphase flow is two-phase flow, which encompasses a range of combinations, including solid-liquid, liquid-liquid, gas-solid, and gas-liquid or bubbly flows. Within the realm of two-phase flow models, there are two primary classifications: separated flow models and homogeneous flow models. In the separated flow model, each phase is allocated a specific region within the flow field with distinct velocity and temperature. Hence, separate sets of governing equations for two phases must be formulated, and the boundary conditions at the interface must be appropriately matched for each phase. However, in a homogeneous flow model, the velocity and temperature of one phase are assumed to be identical to the other phase [42]. Consequently, both phases share only one set of governing equations. According to Ishii and Hibiki [43], two-phase flows are classified on the

basis of the structure of interfaces into several flow regimes, which is demonstrated in 2.1(originally published in the work of Sommerfeld [44])

- Separated flows: The phases are spatially disconnected from each other, like stratified flows, film flows, annular flows, or jet flows.
- Dispersed flows:
  - **Homogeneous flow** represents the asymptotic limit of a dispersed flow, where the dispersed phase is distributed as an infinite number of sufficiently small particles, bubbles, or droplets. This limitation implies zero relative motion between the phases.
  - **Bubbly flow or mist flow** is characterized by a highly dispersed state, and many bubbly flows approach this threshold closely and can be regarded as homogeneous.
- Transitional flows: Between separated flows and dispersed flows, there are numerous transient flow types, for example, where a pure liquid evaporates into steam as a result of external heating.

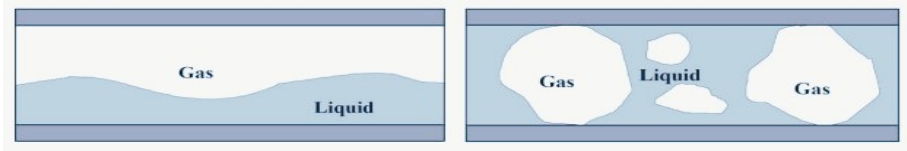

(a) Separated flows

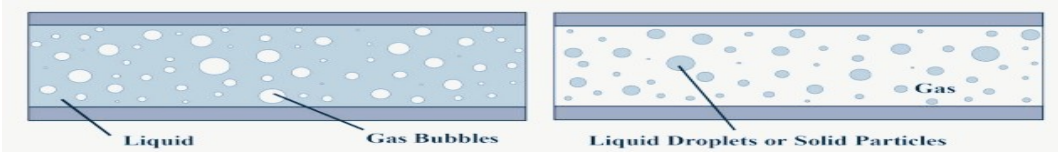

(b) Dispersed flows

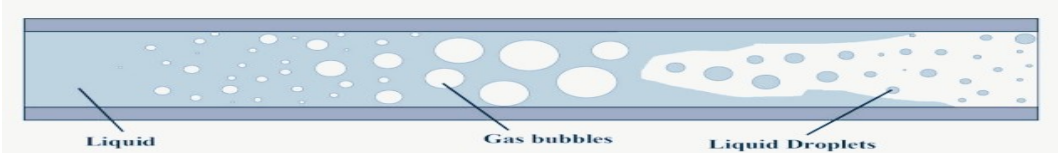

(c) Transitional flows

Figure 2.1: Two phase flows classification and regimes (images taken from [44])

2.2 Homogeneous flow

The present work concerns the modeling and numerical simulation of dispersed two-phase flows. As mentioned earlier, the homogeneous flow model assumes that both phases move at the same speed and mix well and hence can be treated as one phase. The model is more effective when the differences between the properties of liquid and vapor are minimal or when the momentum of the two-phase flow is high enough that the flow regime is either bubbly or misty.

2.2.1 Governing equations of homogeneous flow

Consider the two-phase inviscid flow. The fluid flow dynamics is governed by the continuity equation and the momentum equation for each phase as:

$$\frac{\partial \alpha_p \rho_p}{\partial t} + \nabla \cdot (\alpha_p \rho_p \mathbf{u}_p) = 0, \tag{2.1}$$

$$\frac{\partial \alpha_p \rho_p \mathbf{u}_p}{\partial t} + \nabla \cdot (\alpha_p \rho_p \mathbf{u}_p \mathbf{u}_p) = -\alpha_p \nabla P + \mathbf{F}_i, \tag{2.2}$$

where α is the volume fraction, u is the velocity, P is the pressure, ρ is density and t is the time. The subscript p refers to each phase. $\mathbf{F}_i$ refers to the interfacial momentum transfer term. Here, the surface tension is ignored so that the index $'p'$ could be moved out from P_p, as shown in the first term at the right-hand side of Eq. (2.2).

In a homogeneous flow, $\mathbf{F}_i$ is so large that the relative velocity is neglected, so we have

$$\mathbf{u} = \mathbf{u}_1 = \mathbf{u}_2$$

which simplifies the governing equations, i.e., mass equations, into a single phase form as:

$$\frac{\partial \alpha \rho}{\partial t} + \nabla \cdot (\alpha \rho_p \mathbf{u}) = 0 \tag{2.3}$$

and momentum equation as

$$\frac{\partial \rho \mathbf{u}}{\partial t} + \nabla \cdot (\rho \mathbf{u}\mathbf{u}) = -\nabla p \tag{2.4}$$

2.2.2 Speed of sound in dispersed homogeneous flow

Introducing small variations to the parameters into Eq. (2.3) and (2.4) and neglecting convective terms, we have

$$\frac{\partial \alpha\prime}{\partial t} + \frac{\alpha}{\rho}\frac{\partial \rho'}{\partial t} = -\nabla \cdot (\alpha \mathbf{u}') \tag{2.5}$$

$$\rho \frac{\partial \mathbf{u}'}{\partial t} + \nabla P' = 0 \tag{2.6}$$

where

$$\rho = \alpha_1 \rho_1 + \alpha_2 \rho_2$$

The subscripts 1 and 2 refer to the two phases, i.e., liquid and gas phases,

As in single-phase flows, the existence of a barotropic relation, $P = f(\rho)$, would complete the system of equations Hence, the associated sound speed defined as

$$c^2 = \left(\frac{dP}{d\rho}\right)_Q \tag{2.7}$$

where Q is the thermodynamic constraint. By substituting the Eq. 2.7 in Eq. 2.3 we have

$$\frac{\partial P'}{\partial t} = -K \nabla \cdot \mathbf{u}' \tag{2.8}$$

where we define the effective modulus of the two-phase medium K as

$$\frac{1}{K} = \frac{\alpha_1}{K_1} + \frac{\alpha_2}{K_2}$$

Combining the linearized equation Eqs. (2.8) and (2.4), we get the following wave equation

$$\frac{\partial^2 P'}{\partial t^2} = \frac{K}{\rho} \nabla^2 P' \tag{2.9}$$

Thus, the speed of sound in the two-phase homogeneous flow could be written as

$$\frac{1}{c^2} = (\alpha_1 \rho_1 + \alpha_2 \rho_2) \left(\frac{\alpha_1}{\rho_1 c_1^2} + \frac{\alpha_2}{\rho_2 c_2^2}\right) \tag{2.10}$$

The detailed derivation could be found in [45].

The above equation is equivalent to the well-known Wood's 1930 equation [34] that estimates the speed of sound in a liquid with bubbles at low frequencies based on its

void fraction α. In Wood's formulation, the α is defined as

$$\alpha = V_1/V_m,$$

where V_g is the volume of the gas phase and V_m is the total volume of the mixture, given by $V_m = V_1 + V_2$. The effective mixture density is

$$\rho_m = (1-\alpha)\rho_1 + \alpha\rho_2,$$

where ρ_1 is the density of the gas and ρ_2 is the density of the liquid.

Hence we can write Eq. 2.11 as

$$\frac{1}{c_m} = (\alpha\rho_1 + (1-\alpha)\rho_2)\left(\frac{\alpha}{\rho_1 c_1^2} + \frac{1-\alpha}{\rho_2 c_2^2}\right) \tag{2.11}$$

In our study, understanding the distribution of the speed of sound within the two phases is essential for calculating the propagation of acoustic waves. This computation is carried out independently using a dedicated propagation model. Therefore, we will utilize the derived equation for the speed of sound, as it offers valuable insights.

2.3 Numerical approaches for two-phase flows

The numerical calculation of multi or two-phase flows often involves two predominant approaches:

- Euler-Lagrange approach
- Euler-Euler or two-fluid approach.

In the Euler-Lagrange approach, the carrier phase is treated continuously, while the dispersed entities are approximated as individual mass points and tracked independently. Each entity is represented by Newton's equation of motion.

The Euler-Euler approach, a widely used technique, sets up transport laws based on the volume fractions of the two phases in every computational control volume. This leads to a continuous representation of both phases, each occupying a certain volume within the computational domain. To satisfy conservation laws, the flow fields of both phases are weighted by their volume fractions in each control volume. As a closure relation, the total volume fractions within each control volume combine to equal one.

For dispersed multi-phase flows, two concepts are possible: the mixture or homogeneous approach and the two multi-fluid methods. The mixture model is a simplified

form of the Euler-Euler approach, where the conservation equations for the mixture are solved, implying that no interfacial transfer terms appear in these equations. The mixture model can be further divided into the homogeneous mixture model, where both phases share the same velocity and a model where a relative or slip velocity is considered using algebraic slip formulations.

The volume of fluid method (VoF) [46] uses the homogeneous modeling approach. It is an algorithm for the interface tracking of two or more immiscible fluids, where a single set of momentum equations is applicable to all the fluids and relies on a volume fraction indicator α to identify the location of the interfaces of different phases in all cells of a computational domain. A value of 0 signifies an empty cell, while a value of 1 indicates complete filling. Intermediate values denote the presence of a free (interface) boundary within the cell. In essence, the volume fraction of water (α) is calculated as the water volume ratio to the total cell volume, with $(1 - \alpha)$ representing the volume fraction of the second phase, such as air.

In this work, a homogeneous mixture model is chosen, and the volume of fluid approach for the numerical simulations is considered.

2.3.1 Homogeneous mixture model

It is imperative to carefully select the appropriate model to accurately model fluid flow, considering factors such as flow conditions, physical properties, computing resources, and precision level. We considered the homogeneous mixture model with a volume fraction approach and assumed that the vapor (air) is finely dispersed throughout the liquid (water) without undergoing any phase changes; consequently, the air-bubble layer will be referred to as the air layer for simplicity. The air content dispersed within the fluid is described numerically by a scalar field called vapor or volumetric mixture fraction α inside each computational cell and is defined as:

$$\alpha = \frac{V_{vap}}{V_{tot}}, \tag{2.12}$$

where V_{tot} is the total volume of the mixture and V_{vap} is the volume of vapour dispersed within V_{tot}. The air-water mixture is treated as a homogeneous medium (m) with variable density ρ_m and viscosity μ_m and it is defined in terms of α as

$$\rho_m = \alpha\rho_w + (1 - \alpha)\rho_a \tag{2.13}$$

$$\mu_m = \alpha\mu_w + (1 - \alpha)\mu_a \tag{2.14}$$

where, ρ_w and ρ_a are the densities, and μ_w and μ_a are the dynamic viscosity of water and air respectively. The equations governing the dynamics of two-phase flows are the Navier-Stokes equations, along with the volume fraction transport equation. For an incompressible two-phase flow, the mass conservation equation is

$$\frac{\partial \rho_m}{\partial t} + \nabla \cdot (\rho_m \boldsymbol{u}) = 0 \tag{2.15}$$

and momentum conservation equation for homogeneous mixture can be written as

$$\frac{\partial (\rho_m \mathbf{u})}{\partial t} + \nabla \cdot (\rho_m \mathbf{u}\mathbf{u}) = -\nabla p + \nabla \cdot \mu_m \nabla \mathbf{u} + \rho \mathbf{g} \tag{2.16}$$

where $\boldsymbol{u}$ is the velocity vector, p is the hydrodynamic pressure and g is the gravitational acceleration constant. The transport equation for the air volume fraction (α) read as:

$$\frac{\partial \alpha}{\partial t} + \nabla \cdot (\mathbf{u}\alpha) = 0 \tag{2.17}$$

The equation is homogeneous because we are considering a non-condensable gas. In the case of a condensable gas (like vapor), a source and a sink term, respectively, intended to represent the condensation and vaporization processes of the vapor fraction are added on the right-hand side of Eq.2.17 (see [47] and literature therein reported). The above equations are coded in OpenFOAM using the interFoam solver (the VOF-based interface capturing code).

2.4 Numerical techniques to simulate turbulent flows

Turbulent flows are distinguished by the presence of a broad range of lengths and time scales that span from the smallest, the *Kolmogorov scale*, to the largest, which can be subjected to the geometry [48]. The progress in obtaining numerical solutions of the *Navier-Stokes* equations for high *Reynolds number* turbulent flows, under the constraints of computer resources and time, continues to be a major focus of research. The following frameworks upto date are considered to numerically handle the turbulent flows: *Reynolds Averaged Navier Stokes* (**RANS**), *Direct Numerical Simulation* (**DNS**), *Large Eddy Simulation* (**LES**) and the emerging approach *Wall modeled Large Eddy Simulation* (**WMLES**).

The first and the most popular approach is the set of RANS equations, which involves Reynolds decomposition [49]. This decomposition replaces the instantaneous quantities with time-averaging and fluctuating components. RANS-based approaches are widely used in industries due to their low cost. However, the RANS approach

has limitations, i.e., its impotence to predict complex swirling flows,

In the DNS approach, the turbulent flows are simulated directly in time and space, meaning that the Navier-Stokes equations are solved without approximating the quantities into time average and fluctuations [50]. The whole range of spatio-temporal, i.e., from the Kolmogorov microscale to the integral scale related to the motions carrying the majority of the kinetic energy, are resolved in DNS. It is the most accurate approach for simulating turbulent flows. However, due to expensive computational cost, it is impractical for flows with high Reynolds numbers.

LES is the scale-resolving numerical simulation approach of turbulent flow in which large eddies are computed directly while small eddies are modeled. The LES shows significant potential for the under-resolved but precise simulation of complex flows. The equations are modeled by setting the filter up to a specific length scale Δ, which is equal to the local computational cell size. The length scales which are smaller than the width Δ are represented by the Sub-Grid-Scale (SGS) model [51]. The LES model consumes less computational cost than the DNS.

The computational expenses of LES can be significantly reduced by using wall-modeled LES (WMLES). In wall-modeled LES, turbulence far from the wall is estimated using LES, and the flow close to the wall is determined by employing a reduced-order model on a relatively coarser grid that manages the effect of energetic near-wall eddies. [52].WMLES utilizes the following two approaches: "wall-stress modeling" and a "hybrid of RANS and LES." The difference between these approaches is related to LES interaction with near-wall turbulence that leads to unique flow patterns and modeling challenges [53, 52]. In spite of differences, both methods commonly encounter the issue of a vertical shift in the inner scaled mean stream velocity profile, referred to as log-layer mismatch LLM. For a detailed discussion of this chronic issue, see [52, 54, 55]. However, many more investigations are still needed to make WMLES more reliable and effective.

This work considers the two CFD simulations, particularly focusing on channel flow and flat plate. The one with LES at low Reynolds number and the other one with the WMLES to handle very high Reynolds numbers without excessive computational costs. Note that the Wall-Adapting Local Eddy-viscosity (WALE) turbulence model is employed to resolve the sub-grid scale tensor [56].

Chapter 3

Turbulent Numerical Simulations of Air Injection

The objective is to simulate a realistic distribution of the air-bubble layer or air layer over the plate rather than characterize the flow property. The model we consider to simulate the flow with air injection is presented in 2.3.1. Firstly, this chapter explores the simulation of a two-phase flow, beginning with an examination of a laminar flow channel as a test case. This test assesses the performance of the interFoam solver, particularly when injecting air near the top wall. Next, we will investigate turbulent flows and the injection of air through two different scenarios. In one scenario, the air layer is generated at a low Reynolds number (LRN); in the other, it is generated with a high Reynolds number (HRN). These simulations will utilize large eddy (LES) and wall-modeled large eddy simulation (WMLES). CFD numerical simulations are performed in two steps. The first step sets up a simulation to develop fluid flow, while the second step injects air into the domain after the flow is developed. The ultimate state of the flow consists of an air-water mixture layer and water.

3.1 Test case: Injection of air in laminar flow

Poiseuille's theory shows that the incompressible laminar fully developed Newtonian fluid flow within a constant channel exhibits a steady parabolic velocity profile. We want to inject air into this fully developed numerical flow.

3.1.1 Simulation setup

We consider flow a of a Newtonian fluid with density ρ and viscosity ν between two parallel stationary plates, These plates are considered as wall and no-slip condition is applied The dimensions of the domain is $(1 \times 0.1 \times\ 0.1)$m in $x, y$and z direction respectively. Fluid is introduced with a parabolic profile with average velocity $U_{avg} = 1m/s$ in the positive x-direction at the inlet and imposed in a forcing body

force term driving the flow. The description of boundary conditions are given in table (3.1). The distance between the plates is h and set to 0.1 m for this case. The

Parameters	Inlet	outlet	top wall	bottom wall
U	parabolic	zero gradient	no slip	no slip
p_{rgh}	zero gradient	zero gradient	uniform 0	zero gradient
alpha.water	custom	zero gradient	zero gradient	zeroGradient

Table 3.1

interFoam solver is used and hence implemented a boundary condition on a scalar field α, also known as volume fraction, for introducing the air. We consider the thickness of air layer λ_a =0.02m and setting the $\alpha = 0$ that is "pure air" and when $h > \lambda_a$, α goes to 1 that is "water". We inject the air when the flow is fully developed.

The volume fraction α inside the two-phase domain along a wall is shown in figure (3.1). It is observed that inside the thickness of the layer, the volume fraction decreases, then increases steadily and approaches the water, hence termed the "air-water mixture layer". The parabolic profile turns out to be as shown in figure (3.2).

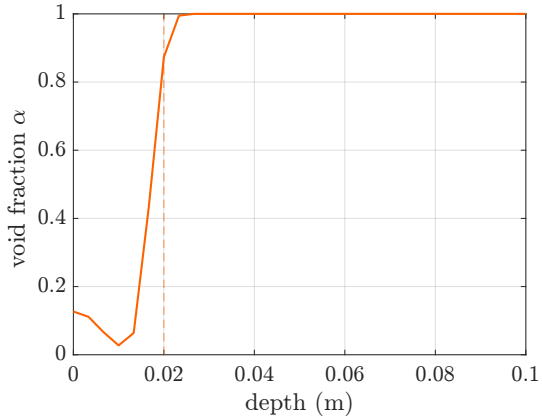

Figure 3.1: Mean volume fraction

It can be seen that the presence of the air inlet changes the flow velocity near the wall. It increases within the layer and then declines as it moves further. This is simply a test case to check the performance of considering the air layer inlet using the interFoam solver. In the next sections, a more comprehensive analysis can be seen for cases with realistic conditions.

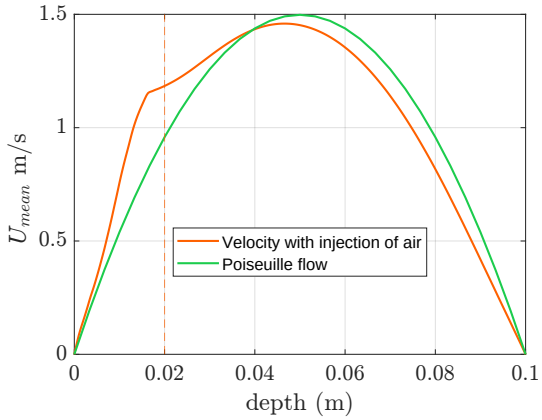

Figure 3.2: Mean velocity profile of the single-phase Poiseuille flow and the two-phase air inlet flow.

3.2 Air-water mixture layer at low Reynolds number (LRN)

This section provides comprehensive details on the numerical setup and a concise discussion in subsection 3.2.1 regarding the fluid dynamic results achieved using the mixture model. As previously mentioned, we leverage the gas-phase distribution to derive the density and speed of sound distributions utilized in the subsequent wave-propagation phase. A process elaborated further in subsection 5.1.

3.2.1 Turbulent channel flow with air injection

A large eddy Simulation (LES) of a turbulence channel flow is performed. The numerical simulation is carried out in two steps: first, a single-phase channel flow is simulated to achieve a fully developed turbulent flow, and then air is injected into the domain, enabling the development of the air layer. The Reynolds number $Re_\tau = u_\tau \delta/\nu \approx 180$, where u_τ is the friction velocity, δ is the semi-height of the channel and ν is the kinematic viscosity, is based on the single-phase simulation, which reproduces the benchmark case [50]. The size of the channel is $4\pi \times 4/3\pi \times 2$ (m), shortened in the spanwise direction with respect to [50] to reduce the computational cost. Therefore, the semi-height of the channel is $\delta = 1$. The desired $Re_\tau = 180$ is obtained setting $\nu = 1/180$ since the $u_\tau = 1$.

The physical domain is discretized using a cartesian grid with $64 \times 64 \times 146$ cells in the streamwise (x), spanwise (y), and wall-normal (z) directions, respectively. The spatial resolution is uniform in the x-y direction, i.e., in wall unit $\Delta x^+ \approx 35$ and $\Delta y^+ \approx 11.7$. In the z-direction, the cell-to-cell aspect ratio starting from a wall up to the middle of the channel is fixed to $\Delta z^+_{i+1}/\Delta z^+_i \approx 1.022$, and the first cell

center from the wall is positioned at $\Delta z^+ \approx 0.5$ to correctly resolve the fluid-dynamic viscous layer KimMM87. Periodic boundary conditions are applied to the lateral boundaries, while a no-slip condition is enforced at the top and bottom walls. The flow is driven by imposing a forcing term in the momentum equations determined from the bulk velocity of $u_b = 15.63\,\mathrm{m\,s^{-1}}$. The non-dimensional time step of the simulation is $0.000\,49 u_\tau/\delta$, and the period over which the data are collected extends up to $T = 6u_\tau/\delta$. The validation of the single-phase simulation is briefly reported here.

The comparison of the first and second-order statistics of $Re_\tau = 180$ water channel flow between the current simulation and the results from [50] is shown in the next two figures. The mean velocity profile in wall units is shown in figure (3.3). In our case, the wall-normal direction is z, compared to the classical y direction.

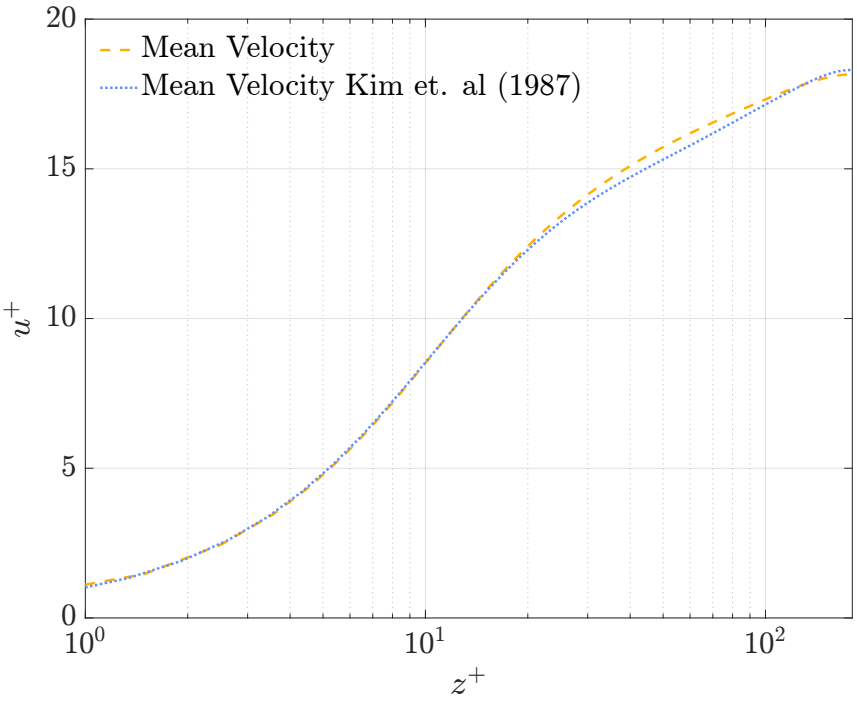

Figure 3.3: Mean streamwise velocity component along the wall-normal direction of of the plain channel flow at $Re_\tau = 180$.

The present simulation can correctly capture the behavior of the mean velocity profile in the viscous sublayer. Small differences arise at the end of the buffer layer, slightly overestimating the mean velocity. This is due to the reason that the resolution in streamwise and spanwise direction are lower in comparison to the [50].

In Figure 3.4, we show the turbulence intensities calculated by the present simulation

and the results obtained by [50], labeled with the K. The results show that our

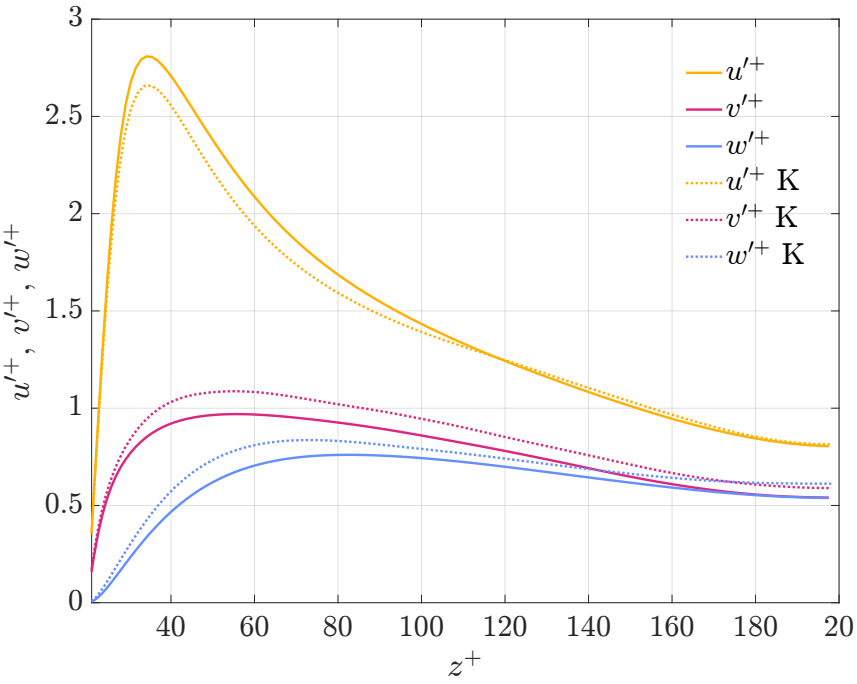

Figure 3.4: Root-mean-square velocity fluctuations normalized by the wall shear velocity of the turbulent channel flow $Re_\tau = 180$. The dotted lines (K) are the results from [50].

simulation slightly overestimates the velocity fluctuations in the buffer layer before converging to the results of [50] along the length of the channel for the wall-normal and the spanwise component and underestimates the streamwise fluctuations in the same region.

3.2.2 Air injection

In the air injection case, the air velocity is set to be the same as that used in the water channel case by utilizing the outlet velocity data. The zero gradient boundary conditions are set at the outlet of the domain. We collected the outlet boundary velocity data for a time window equal to 100 non-dimensional time units. The necessity of collecting the boundary data depends on the characteristics of the new numerical experiment, which involves imposing an air inlet on a section of the inlet boundary since we need to prevent the re-entry of gas flow at the outlet into the inlet (cyclic boundary condition). Indeed, imposing a multi-phase inlet condition prevents the adoption of cyclic boundary conditions, so a turbulent velocity inlet is also necessary.

3.2.2.1 Procedure to generate inflow velocity field

The approach is to extract instantaneous planes of velocity data from a single-phase turbulent channel flow. We get the last instance of the already turbulent flow and use it to create the planes as boundary data. This is achieved by utilizing the Openfoam inbuilt boundary condition "timeVaryingMappedFixedValue" for velocity. This will create the velocity values at every instance for the next simulation, in our case, an air injection simulation.

3.2.2.2 Adjustment of the parameters

The air is injected at the inlet section of the domain, adjusting the parameter α, the volume fraction term, by setting it to 0 in the proximity of the top boundary, representing air, and 1 on the remaining section, representing water. Specifically, the air thickness is 0.1δ. The numerical experiment is carried out using the multi-phase solver.

The simulation's time step is adjusted to maintain the Courant number below 0.1 for stability reasons. Due to the velocity reduction in the boundary layer, the air-water mixture takes about 100 non-dimensional time units to reach the outlet boundary. Thus, the two-phase channel flow required significantly more time than the single-phase channel flow to reach a statistically steady flow across the length of the channel.

The air density ρ_{air} is set to $1\,\mathrm{kg\,m^{-3}}$ while the water density ρ_{water} is $1000\,\mathrm{kg\,m^{-3}}$. The kinematic viscosity of the water is fixed to $\nu = 180$ to achieve the correct single-phase Re_τ. Consequently, the kinematic viscosity of the air is fixed accordingly to keep the same ratio between the real media.

3.2.3 Findings

The temporal evolution of the water volume fraction (α) shows significant variability along the spanwise direction. In particular, we observe the presence of gas streaks aligned with the flow direction, which is likely attributed to the inherent vorticity of the turbulent channel near the wall. For illustrative purposes, we present three different snapshots of the turbulent channel, highlighting the vapor phase distribution using the α =0.25 isosurface (Figure 3.5).

In realistic conditions, the acoustic signal propagates while the air phase evolves over time with the fluid flow. Therefore, the incident waves on the plate encounter a continuously varying air distribution. In principle, this is something that can be implemented in a propagation model rather straightforwardly. However, as a preliminary analysis in this study, we opted for two simplified conditions: i) in the first, we consider an instantaneous field of α (specifically, an instantaneous field obtained at the end of the multi-phase simulation), held constant over time while observing the propagation of acoustic waves; ii) in the second, we use the average distribution of α, calculated over time and space. Hereafter, we refer to these two conditions as *Heterogeneous instantaneous field* and *Heterogeneous mean field*.

In figure (3.6), the contour map of α depicts the instantaneous distribution of the air-water mixture taken at a final time window of the simulation (top panel) and its average profile in time and space (bottom panel). The α values presented in the following Figures have been interpolated to a grid with the same grid points of the LES simulation but with equal spacing along all directions. For the instantaneous α field (Fig.3.6a), we selected the $x - z$ plane at the center of the channel ($y = 2\pi/3$). We observed that the thickness of the air reduces rapidly and then expands, forming a cloud. As the cloud moves towards the end of the channel, it reduces in size and collapses into a tiny air layer. However, at the end of the channel, the air layer appears to expand again. It is important to note that there is significant variability along the spanwise direction, and this particular section may not be representative of the entire distribution of the gas. This is evident in the distribution of the mean values of α (shown in Fig.3.6b), which displays a nearly uniform thickness of the air layer across the length of the channel.

To enhance the visualization of the variability of the air concentration along the domain, we extracted the values of α along different vertical lines, considering the last instantaneous field (α_{inst}) and the mean-field (α_{mean}), in Figure 3.7. The instantaneous field results are shown over lines that are located at mid-channel in the spanwise direction and in $x = \pi, 2\pi, 3\pi$. The black vertical line in the Figure denotes the thickness of the air layer at the inlet (0.1 m).

(a)

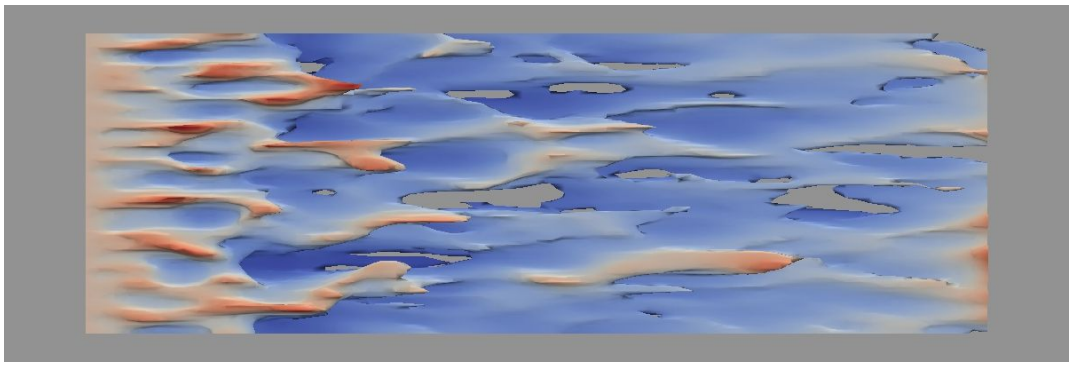

(b)

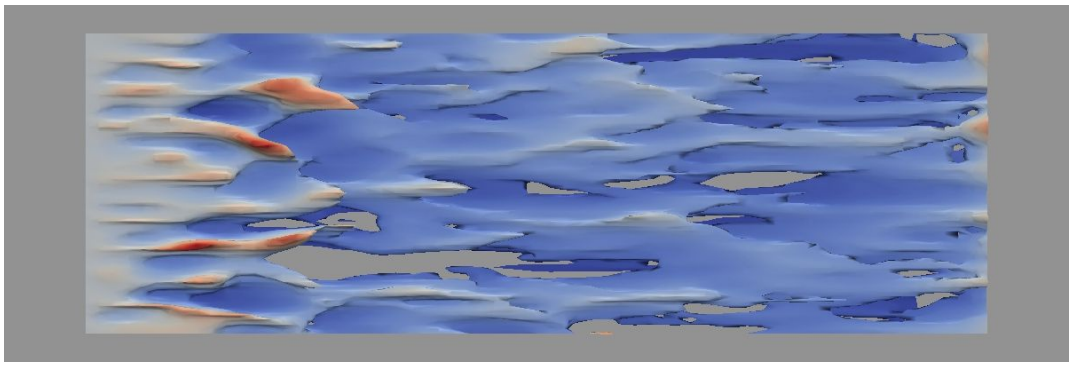

(c)

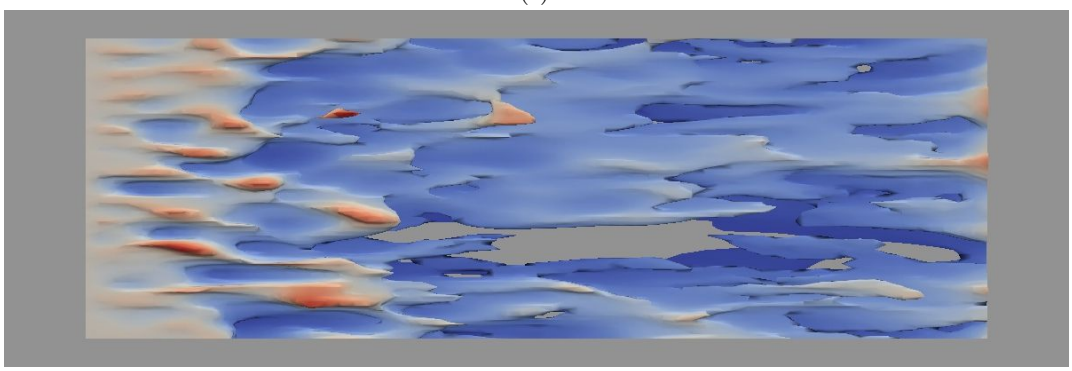

Figure 3.5: Instantaneous isosurface of α =0.25, taken at (a) 40 s and (b) 60 s (c) 80 s

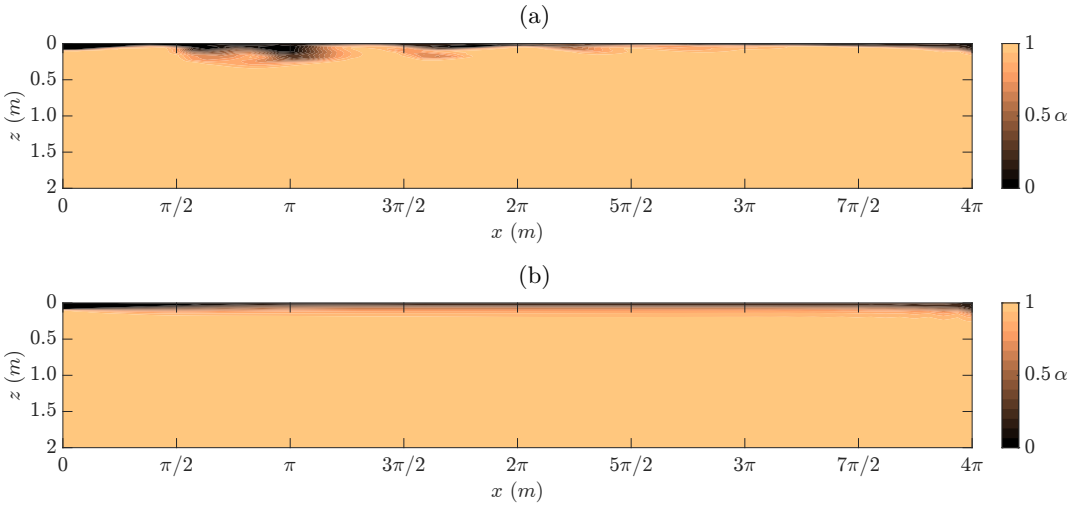

Figure 3.6: Contour of the water volume fraction α: a) instantaneous field in the x-z plane at the center of the channel ($y = 2\pi/3$); b) mean field in the x-z plane of the channel.

While the distribution over some lines may be comparable (see lines at $x = 2\pi$ and $x = 3\pi$), the line at $\alpha = \pi$ clearly shows a major content of air distributed along the vertical line, which is reasonable being closer to the inlet. The mean distribution of α reasonably mitigates the instantaneous field's abrupt changes and uneven variations.

3.2.4 Analysis of air-to-water transition

We pay attention to the air-to-water transition, which may happen differently, although all the lines clearly exhibit a region of air-water mixture. This region is significant since the minimum speed of sound is reached at $\alpha = 0.5$, as mentioned above. We note that the instantaneous field distribution may have a sharper transition with respect to the average field; see lines at $x = 2\pi$ and $x = 3\pi$. In this case, the minimum value of $\alpha = 0.2$ is reached in less than $0.05\,m$. On the other hand, towards the inlet section of the channel, a completely different gradient of α is observed, as represented by the line extracted at $x = \pi$. The mean field distribution is somewhat in between the two scenarios: the mixture region starts at about $z = 0.15$, then α reaches its minimum value of 0.25 at $z \sim 0.02$, and subsequently rises until it reaches 0.3 at the wall.

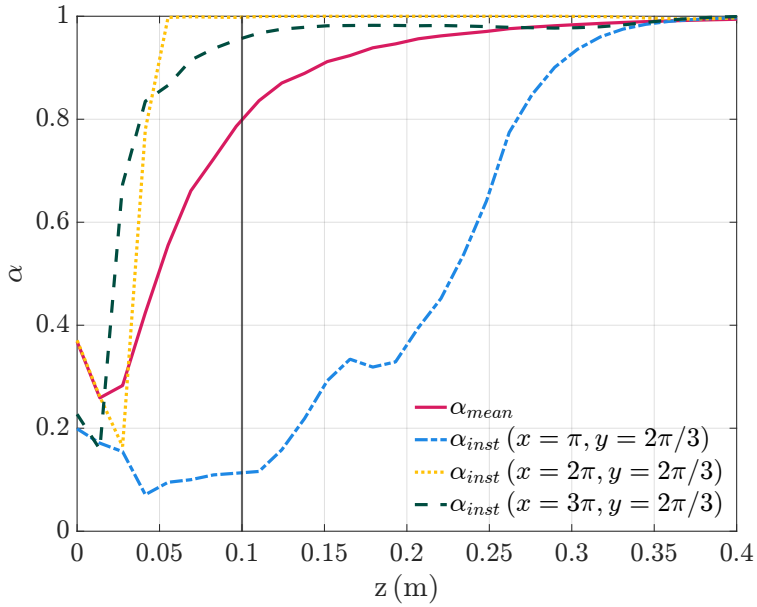

Figure 3.7: Instantaneous and mean field distribution of water volume fraction (α) along the wall-normal direction at different distances from the inlet.

3.2.4.1 Formulation of density and speed distribution

We exploit this scalar field α to compute the distribution of density and speed of sound within the domain. The density of the mixture ρ_m is evaluated through equation 2.13, while the speed of sound for the mixture c_m is determined considering Wood's formulation (see also, section 2.2.2):

$$\frac{1}{c_m^2} = \frac{(1-\alpha)^2}{c_a^2} + \frac{(\alpha)^2}{c_w^2} + \alpha(1-\alpha)\frac{\rho_a^2 c_a^2 + \rho_w^2 c_w^2}{\rho_l \rho_a c_w^2 c_a^2}, \tag{3.1}$$

where ρ_w =1000 kg m^{-3}, ρ_a =1 kg m^{-3}, c_w =1500 m s^{-1} and c_a =330 m s^{-1}.

Wood's equation (3.1) rules the speed of sound of bubbly flows, varying according to the air fraction; we report its profile in Figure 3.8. It can be seen that the speed of sound rapidly decreases as the medium becomes a mixture, reaching a minimum sound speed of about 20.86 m s^{-1} at $\alpha = 0.5$. We opted for Wood's equation due to its applicability to isothermal processes, which aligns with the condition considered in our case.

Hence, the profile of c_m along the vertical lines is computed through Wood's equation 3.1, and it is reported in figure 3.9.

The non-linear dependency of c_m with respect to α is visible. Moreover, we stress the fact that a small variation of α with respect to the boundary values $\alpha = 0$ or $\alpha = 1$

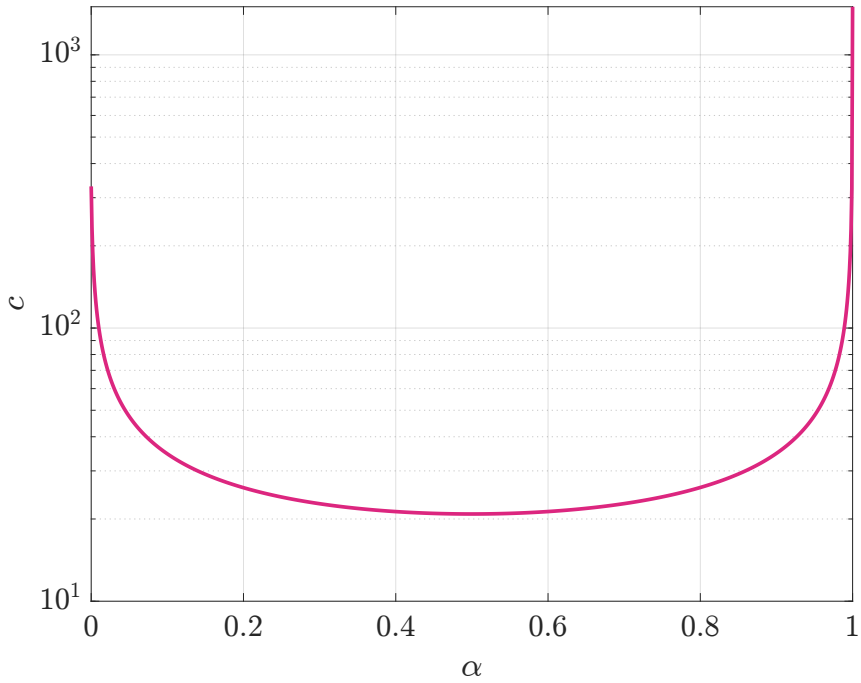

Figure 3.8: Sound speed (c_m) [$\mathrm{m\,s^{-1}}$] in a bubbly liquid as a function of volume fraction α, as predicted by Eq. 3.1.

gives rise to a strong variation in the speed of sound. Specifically, the line at $x = 2\pi$ clearly shows this behavior: at depth, $z > 0.1\,m$ the value of α is approximately 1, it deviates from the value of one by a delta on the order of 10^{-3}. This is enough to attain minimum values of c_m around $100\,m/s$. The minimum speed c_{min} observed when considering averaged α is $20.90\,m/s$ whereas for the instantaneous distribution, it stands at $21.86\,m/s$.

Looking at the figure 3.8, it is noticeable that the minimum of c_m is reached in correspondence of $\alpha \sim 0.5$.

Note that the density profile is not reported as ρ_m exhibits a linear dependence on α, aligning its distribution with that of α.

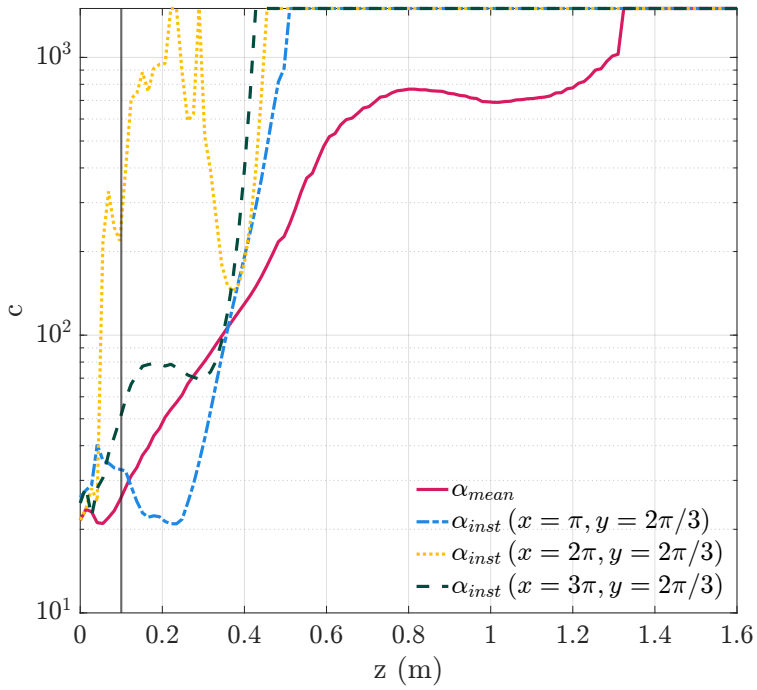

Figure 3.9: Instantaneous and mean field distribution of the speed of sound (c) along the wall-normal direction at different distances from the inlet evaluated from the α distribution (Fig.3.7) using the Wood's equation (3.1).

3.3 Air-water mixture layer at high Reynolds number (HRN)

In this case, we attempted to simulate the air film adhering to the wall under more realistic conditions found in real applications by employing the WMLES. Due to the high Reynolds number, the idea is to evaluate only a section of the channel. We conduct a numerical experiment only on the upper section of the channel, where the air layer is injected to reduce the associated computational cost. The upper flat plate is considered to have a no-slip condition, and the bottom surface of the numerical domain is treated with a slip condition, enabling the flow in the streamwise direction. The cyclic condition is applied for the rest of the surfaces, i.e. (left, right, back, front). This is a limitation compared to the classical full channel. However, we deem it sufficient for the purpose of this research, which is to develop a thin layer of air at this very high Reynolds. In the future, we will also consider the solution for the whole channel to enable the correct transfer of momentum from the wall to the center of the channel. Another option is to consider a case where the flow is induced by the upper wall and not by a pressure gradient, which is better for the case of an immersed object in motion.

The numerical domain is characterized by three dimensions: streamwise $L_x = 0.1m$, spanwise $L_y = 0.1m$, and wall-normal $L_z = 0.02m$. The computation is carried out with 8000000 grid points (200 x 200 x 200) with uniform mesh for a Reynolds number Re_{bulk} of about 2.26e5 ($Re_{tau} \approx 8000$). The Reynolds number is computed as $u_b L_z/\nu_w$, where u_b =11.3 m s^{-1}, L_z height of the domain and ν_w is kinematic viscosity of water.

The WMLES is implemented; hence, the grid spacing in the streamwise and spanwise directions are Δx^+ and $\Delta y^+ \approx 250$ and wall-normal is $\Delta z^+ \approx 50$ in wall units. The spacing is constant over the wall-normal.

The wall boundary condition is used for the turbulent viscosity, which calculates the turbulence kinetic energy at the boundary cells (the first cell is the center of the logarithmic area). Periodic boundary conditions are applied to the lateral boundaries, while a no-slip condition is enforced at the top and considered as a wall, However, the slip condition is applied at the bottom and considered as a symmetry surface. The flow is driven by imposing a forcing term in the momentum equations determined from the bulk velocity of u_b =11.3 m s^{-1}. The courant number is set to 0.5 , and the time of the simulation in which the data are collected are up to $34L_x/u_b$ s, To evaluate the velocity in terms of wall units, we calculated the wall hear stress τ_w using the pressure gradient as

$$\tau_w = \rho h \frac{dp}{dx} \tag{3.2}$$

where dp/dx is the pressure gradient evaluated from the simulation, h is the depth of the domain, i.e., 0.02 m, and ρ is the density of the flow, i.e., ρ_w. From Eq.(3.2) we have then calculated the friction velocity.

$$u_\tau = \sqrt{\frac{\tau_w}{\rho}} \tag{3.3}$$

The value u_τ of the simulation is about 0.354 m/s and hence the $Re_{tau} = L_z u_\tau/\nu$ evaluated here is about 7000.

The mean velocity profile and its comparison in wall units are shown in figures (3.10) and (3.11) respectively.

As mentioned earlier, the WMLES is an efficient way to simulate higher-order Reynolds number numerical experiments. Still, it overestimates the velocity profile, which mismatches the logarithmic law (LLM). This problem is still ongoing, and only a few investigations have been conducted to overcome it.

One of the ideas is to introduce the stochastic forcing in the interface region, first implemented by [57] using the Spalart and Allmaras wall model LES (SA-WMLES) model.

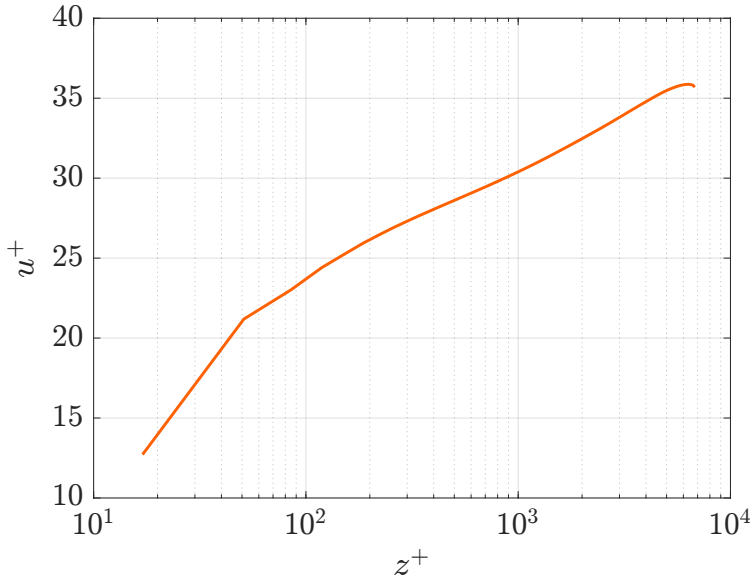

Figure 3.10: Mean velocity profile in wall units of the WMLES at $Re_{tau} = 7000$

At the moment, we are not addressing this problem as our primary focus is on the overall flow rather than the wall stress and fluctuations. Hence, we compare our results in figure (3.11), which shows LLM reduced profiles of mean velocity taken from the [57], to ensure that the flow is approaching $Re_\tau \approx 8000$.

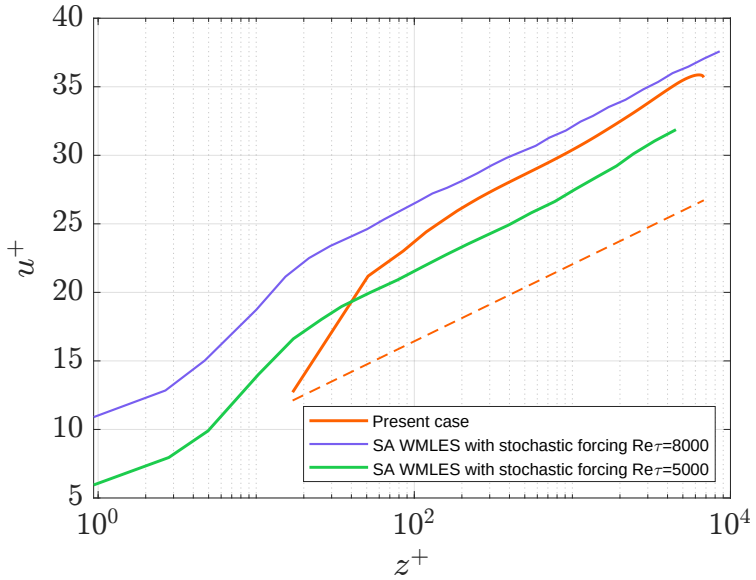

Figure 3.11: Mean velocity profiles in wall units. blue line: Re_τ=8000, SA-WMLES with stochastic forcing, Green line: Re_τ=5000 SA-WMLES with stochastic forcing (These profiles are taken from [52] and Orange line: present case with logarithmic law mismatch, (LLM)

3.3.1 Injection of air

The injection of air remains consistent with the procedure carried out in the previous simulation cases, i.e., the LES case 3.2.2.1. However, in this case, three simulations with different air layers are considered. Two with varying thicknesses: one with layer beginning with pure air, i.e., α set to 0: with a thickness of 0.0022 meters, and the other is twice this size. The third simulation is considered with a thickness of 0.0022m when the layer begins with mixed air, i.e., α is set to 0.5. From now on, we denote the first and second simulation layer that begins with pure air as $\lambda_{a1}\alpha_0$ and $\lambda_{a2}\alpha_0$ and the third simulation layer begins with mix air $\lambda_{a1}\alpha_{0.5}$. The simulations are carried out up till the mixture reaches to the end of the domain, It takes about $22L_x/u_b$ s for $\lambda_{a1}\alpha_0$ and $\lambda_{a2}\alpha_0$ while with $\lambda_{a1}\alpha_{0.5}$ it runs about $6L_x/u_b$ s. The Courant number in these cases is set to 0.5

The physical parameters of this simulation are listed in table 3.2.

Physical quantities	value
Air density ρ_a	$1.293[kg/m^3]$
Water density ρ_w	$1030[kg/m^3]$
Air viscosity ν_a	$1.48e-5[m^2/s]$
Water viscosity ν_w	$1e-6[m^2/s]$

Table 3.2

3.3.2 Findings

The isosurfaces for layers beginning with pure air and mixed air are shown in figures (3.12a) and (3.12b). The isosurfaces of $\alpha = 0.7$ for both layers are taken at the final time of the simulation, which shows significant variability along the spanwise direction The contour map of instantaneous distribution of the air-water mixture taken at a final time window of the simulation of the three cases: a)λ_{a1}, α_0 b) λ_{a2}, α_0 and c) $\lambda_{a1}, \alpha_{0.5}$ are shown in figure 3.13. For the instantaneous field, we selected the x z plane at the center of the channel (y = 0.05 m).

Figure (3.14) shows the contour map of the mean field of α that is average over space and time. One can see the uniform distribution along the streamwise direction in all air layers.

(a)

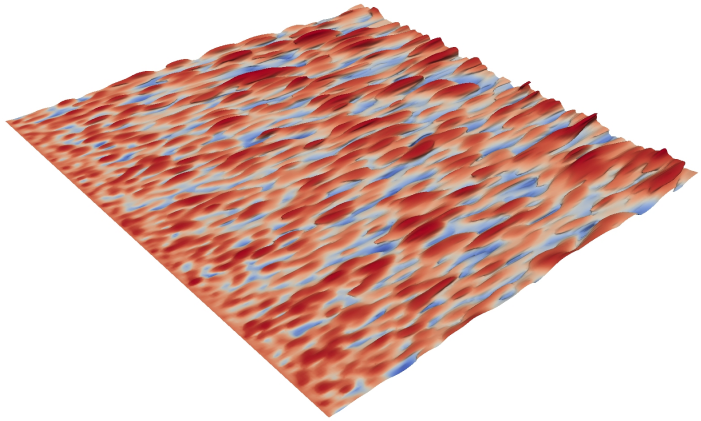

(b)

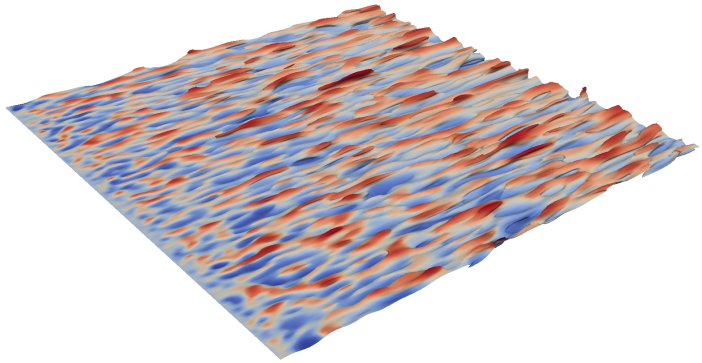

Figure 3.12: Instantaneous isosurface of α =0.7, for: a) λ_{a1}=0.0022 m α_0 and b) λ_{a1}=0.0022 m $\alpha_{0.5}$

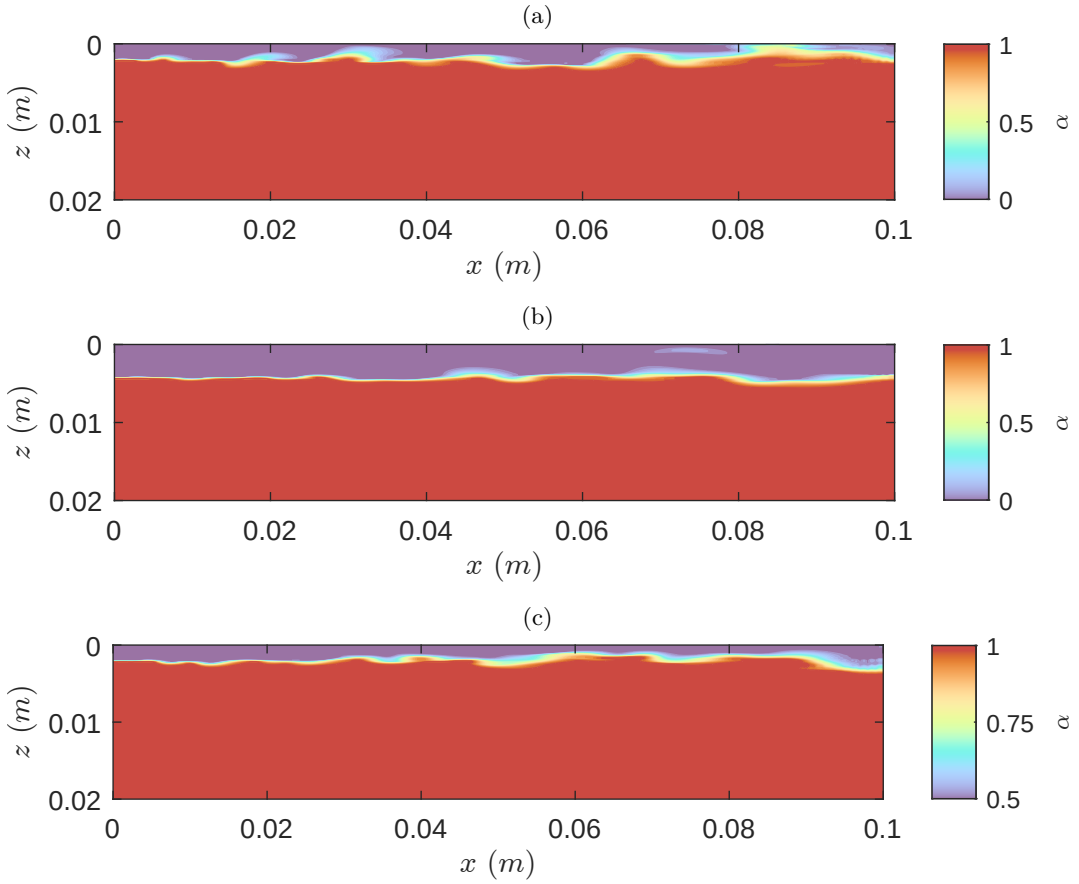

Figure 3.13: Contour of the instantaneous field of volume fraction α in the x-z plane: a) λ_{a1}=0.0022 m α_0 b) λ_{a2}=0.0044 m α_0 and c) λ_{a1}=0.0022 m $\alpha_{0.5}$

Figure (3.15) shows the variation of α along a wall of the domain. It can be clearly observed that the variation of volume fraction with pure air starts with 0 and mixed air with 0.5. The mixture region from right to left start at about $z = 0.005$ for λ_{a1}, α_0 and $z = 0.003$ for λ_{a2}, α_0 , then reaches their minimum value of 0.02 at $z \sim 0.003$ and $z \sim 0.001$ respectively. Then, subsequently rises until λ_{a1}reaches 0.14 and λ_{a2} meets 0.17 at the wall. However, the layer of $\lambda_{a1}, \alpha_{0.5}$ begins near $z = 0.002$ and crossing the minimum value of 0.55 at $z = 0.0005$ and rises again until $\alpha = 0.6$. Considering these distributions of α, we obtained the density and speed of sound of the above mixture layers by adopting the same procedure discussed in section 3.2.4.1. The density profiles due to the linear dependence of these layers are similar to the profile demonstrated for volume fraction 3.15. However, the speed of sound in the domains, utilizing the Woods equation 3.1, takes the form as Figure (3.16). It is evident that

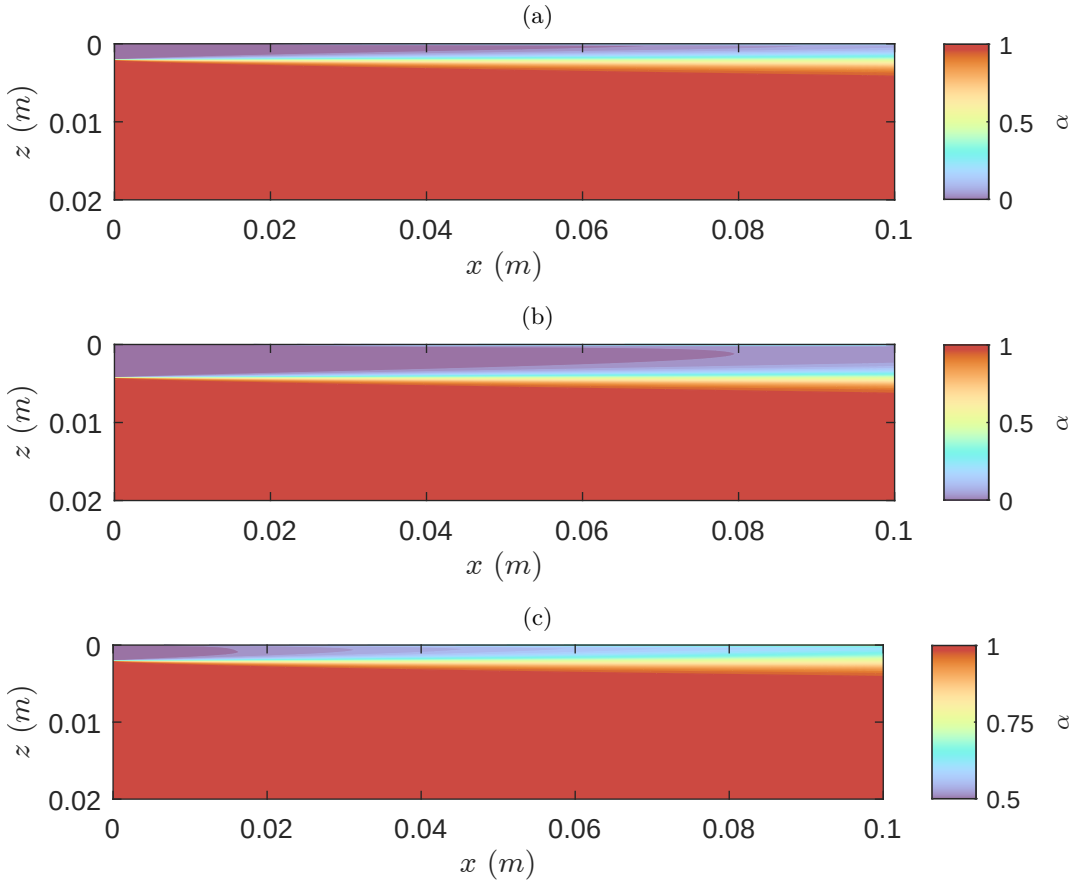

Figure 3.14: Contour of the mean field of volume fraction α in the x-z plane: a) λ_{a1}=0.0022 m α_0 b) λ_{a2}=0.0044 m α_0 and c) λ_{a1}=0.0022 m $\alpha_{0.5}$

the speed of sound in this case follows the behavior illustrated in the figure 3.8. In figure 3.16, the minimum values of α in each layer correspond to a minimum speed that is 20 m/s. For λ_{a1}, α_0 and λ_{a2}, α_0, the speed reaches a minimum, and then it again rises up to 60 m/s. However, for $\lambda_{a1}, \alpha_{0.5}$, there is no variation after the minimum value. This is unsurprising as this layer starts with $\alpha = 0.5$, so there is no variation from 0 to 0.5. Morever, $\lambda_{a1}, \alpha_{0.5}$ exhibits the exact profile as of Woods.

For performing wave propagation in the non-homogeneous medium, we have the distribution of air layers conducting with low and high Reynolds numbers and calculated the density and speed of sound profiles. Hence, in the next chapter, we utilize these key variables and adopt them as input parameters for the acoustic propagation model.

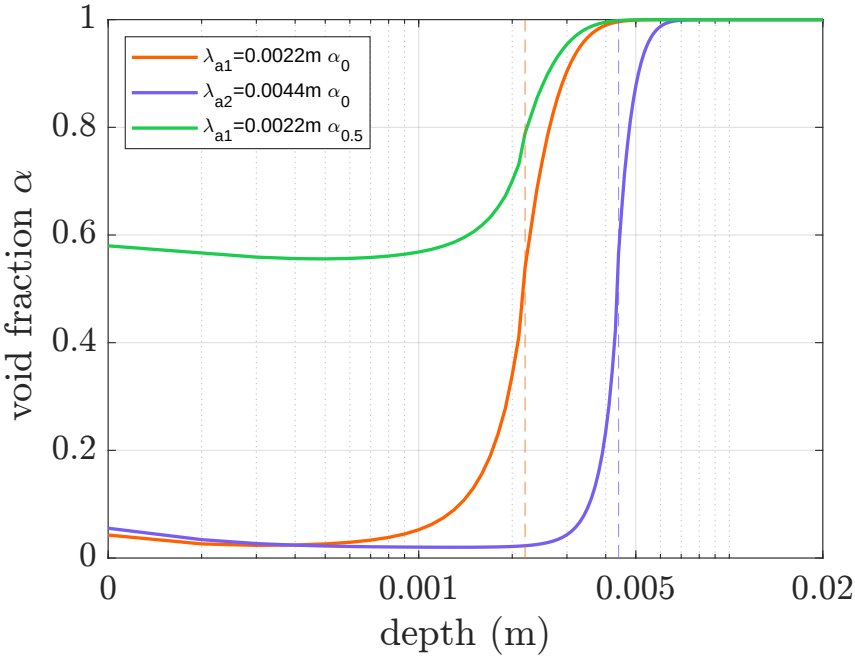

Figure 3.15: Mean field distribution of volume fraction (α) with λ_{a1}=0.0022 m α_0, λ_{a2}=0.0044 m α_0 and λ_{a1}=0.0022 m $\alpha_{0.5}$ along the wall-normal direction

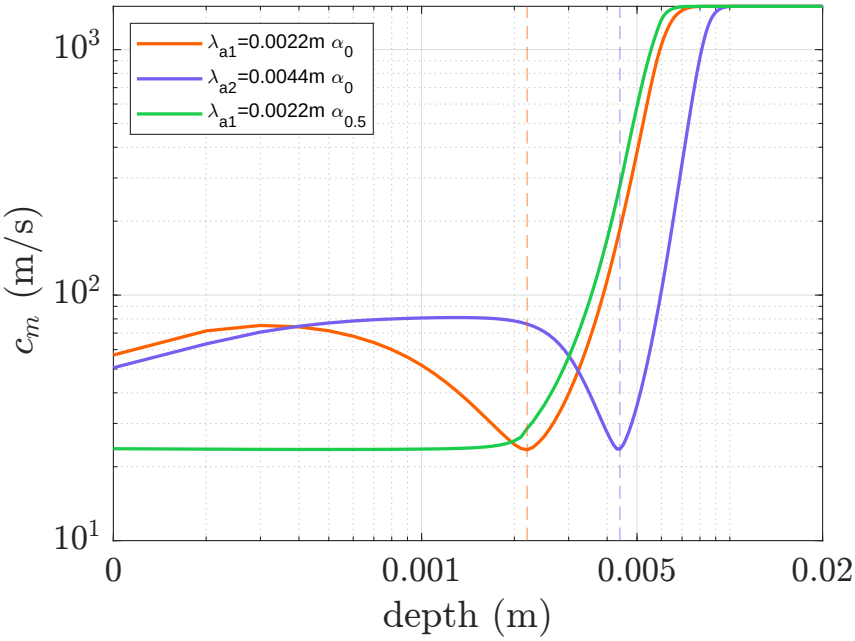

Figure 3.16: Mean field distribution of speed of sound (c) λ_{a1}=0.0022 m α_0, λ_{a2}=0.0044 m α_0 and λ_{a1}=0.0022 m $\alpha_{0.5}$ along the wall-normal direction

Chapter 4

Acoustic Propagation Modeling: Sound absorption in air layer

Underwater noise arises from the propagation of acoustic pressure within the fluid medium. It is influenced by factors such as seafloor morphology, wave-guide properties, and sediment rheology. Despite previous investigations into the three-dimensional (3D) dynamics of acoustic propagation [58],[59], this remains an ongoing area of study due to the complexity of the problem [60].

A variety of acoustic propagation models have been developed in the literature to replicate the underwater sound environment. The selection of a model depends on the specific acoustic scenario being studied [61]. They can be classified by three properties: i) source frequency, ii) environmental dependence (range-independent and range-dependent models), and iii) source location (depending on water depth).

The acoustic wave equation is a mathematical representation of the propagation of sound waves in a medium. The sound propagation wave equation is derived from the hydrodynamic equations by considering the first approximation (linear) of governing fluid equations. Two prevalent approaches are commonly employed for modeling acoustic systems numerically: one involves solving the wave equation directly in the time-space domain. At the same time, the other entails modeling in the frequency domain, leading to the solution of the Helmholtz equation. The Helmholtz propagation approach is widely favored due to its lower computational time compared to solving the wave equation directly in the space-time domain. Hence, this computational efficacy makes the Helmholtz propagation approach an effective method for modeling large-scale acoustic propagation scenarios. However, one of the constraints of the Helmholtz approach is that the equation is generally solved in a two-dimensional (2D) domain. Furthermore, while this method can efficiently handle homogeneous or relatively simple heterogeneous configurations, their application becomes challenging when simulating highly complex media with varying properties in a three-dimensional space.

However, to solve the wave equation in the space-time domain, recent advancements in computational power allow for direct wave equation solutions, albeit in smaller domains and within the low-frequency regime. This approach is particularly suited for scenarios near the coast where three-dimensional environmental effects are significant and for evaluating the interaction between source directivity patterns and the surrounding environment.

In this study, our emphasis is on solving the acoustic wave equation in the space-time domain since the wave equation is three-dimensional.

4.1 Inhomogeneous acoustic wave equation

In underwater acoustics, the pressure variable is of primary interest. Compared to the system of equations involving velocity and pressure, the acoustic wave equation is more easily implemented and numerically solved. It retains most of the advantages, particularly the ability to obtain a detailed space-time map of the acoustic field and implement complex sources in three-dimensional space. The small perturbations of pressure originated by a source are propagated in a medium in the form of waves. Thus, the pressure field p and the density field ρ associated with the pressure field can be written as

$$p = p_0 + p' \tag{4.1}$$

$$\rho = \rho_0 + \rho' \tag{4.2}$$

where p_0 and ρ_0 are the ambient pressure and density fields, respectively, and terms with $'$ indicate the perturbed fields. The continuity equation and Euler's equation (linking pressure, density, and velocity) describe how perturbed density and velocity fields interrelate. To account for localized influences or external forces, a source term is introduced that captures these disturbances. The equations are then simplified by emphasizing the linear terms within the perturbations. Substituting these linearised equations into each other eliminates the velocity field and reveals a second-order partial differential equation governing pressure and density perturbations. This 3D equation takes the form of an inhomogeneous wave equation as

$$\frac{1}{c^2(\mathbf{x})}\frac{\partial^2 p(\mathbf{x},t)}{\partial t^2} = \rho(\mathbf{x})\nabla\left(\frac{1}{\rho(\mathbf{x})}\nabla p(\mathbf{x},t)\right) + S(\mathbf{x},t) \tag{4.3}$$

where c is the local speed of sound, x is the coordinate vector, t is time, and $S(x,t)$ refers to a source function. The detailed derivation of the acoustic wave equation can be found in [62] and [63].

The next section is devoted to the numerical implementation of the acoustic wave equation and the injection of the source. We take advantage of the acoustic solver developed by [64] that solves the three-dimensional acoustic wave equation in the oceanic environment with complex sources.

4.2 Numerical Implementation of acoustic wave equation

Time-domain implementations, particularly using Finite-Difference methods, are widely adopted for their versatility in accommodating media with varying properties. This has made them the preferred technique within the engineering community. Over the past few decades, a plethora of algorithms have been developed, reflecting the widespread use and ongoing development in this field [65],[66]. Among the available discretization schemes, the *finite-difference-time-domain* (FDTD) [67] proves to be highly valuable.

4.2.1 Discrete form of the acoustic wave equation

We consider the acoustic wave equation 4.3 and employ the FDTD method. The computational domain is three-dimensional and Cartesian, consisting of cubic cells with equal lengths in all directions. The algorithm employs a second-order *finite difference scheme* to approximate both time and space derivatives, The discrete form of Eq. (4.3) in one dimension is as follows:

$$\begin{aligned} p_i^n = & -p_i^{n-2} + 2p_i^{n-1} + \frac{\Delta t^2}{\Delta x^2} c_i^2 \rho_i \\ & \left[\frac{1}{2} \left(\frac{1}{\rho_{i+1}} + \frac{1}{\rho_i} \right) \left(p_{i+1}^{n-1} - p_i^{n-1} \right) - \frac{1}{2} \left(\frac{1}{\rho_i} + \frac{1}{\rho_{i-1}} \right) \left(p_i^{n-1} - p_{i-1}^{n-1} \right) \right] + S_i^n. \end{aligned} \tag{4.4}$$

During each iteration n, the acoustic pressure p_i^n at point i is determined. With the length of the domain L_x and n_x cells, positions along x are $\Delta x_i = i\Delta x$. Time is $\Delta T = n\Delta t$ with constant time step Δt. Pressure at time n relies only on values from the two prior time steps, i.e., $n-1$ and $n-2$. Moreover, density ρ_i and speed c_i are defined at each vertex of the cell of the grid. Hence, these two variables vary along the domain. In our case, it is designated by CFD simulation by considering the volume fraction, which has been extensively described in Chapter 3. The source term S is treated according to the specific conditions of the problem at hand (which will be further discussed later in the subsection).

4.2.2 Stability criteria

The time step of the numerical computation is defined by the stability criterion evaluated using the von Neumann criterion:

$$\Delta t \leq (1/c) * \left(1/dx^2 + 1/dy^2 + 1/dz^2\right)^{-1/2} \tag{4.5}$$

The time step of the numerical simulation varies with the cell size. The frequency of the source determines the maximum threshold for the discretization space. In fact, to correctly determine the wave propagation, a minimum number of points is needed to reproduce the source wavelength correctly. In the second-order methods, a minimum of 8 points per wavelength is needed.

4.2.3 Boundary conditions

In order to determine the solution of the wave equation, the boundary conditions are in the following categories: Reflecting and non-reflecting or absorbing boundary conditions.

- Reflecting boundary condition
  - Neumann boundary condition (Free surface condition): When the wave hits the boundary, and the wave is to be reflected back without any phase shift, one applies the Neumann boundary condition that is acquired by applying the derivative of acoustic pressure at the boundary points

    $$\frac{\partial p(\mathrm{x}, \mathbf{t})}{\partial x} = \frac{p_{i+1}^n - p_{i-1}^n}{2\Delta x} = 0 \tag{4.6}$$

    The ghost cells formulation is utilized at the boundary in order to obtain the neighbour points to perform the above equation.
  - Dirichlet boundary condition (Rigid surface condition): The Dirichlet condition is obtained by considering the preferred acoustic pressure value at the boundary points. This condition can be used when dealing with the water-air interface, where the interface represents the pressure-free condition. Hence, the incident wave is reflected back with the phase shift of 180.

    $$p(\mathrm{x}, \mathbf{t}) = p_i^n = 0 \tag{4.7}$$

- Absorbing boundary condition: considering the numerical modeling of acoustic wave propagation in an infinite domain, the actual domain usually exceeds the domain of interest, which can cause a problem in defining a boundary condition,

leading to unwanted reflections on the boundaries. Hence, to simulate such an unbounded medium, absorbing conditions must be defined at the artificial boundaries of the domain. The *perfectly matched layer* (PML) method proposed by [68] is employed to minimize the spurious reflections.

The numerical domain is divided into two sub-regions, the real one and the PML one. The additional term in the PML region is also evaluated in 4.4. Hence the 4.4 can take a form as:

$$\begin{aligned} p_i^n = & -p_i^{n-2} + 2p_i^{n-1} + \frac{\Delta t}{\Delta x^2} c_i^2 \rho_i * \\ & * \left[\frac{1}{2} \left(\frac{1}{\rho_{i+1}} + \frac{1}{\rho_i} \right) \left(p_{i+1}^{n-1} - p_i^{n-1} \right) - \frac{1}{2} \left(\frac{1}{\rho_i} + \frac{1}{\rho_{i-1}} \right) \left(p_i^{n-1} - p_{i-1}^{n-1} \right) \right] + \\ & + \frac{\Delta t^2 \rho_i c_i}{\Delta x} \left(\sigma_i \psi_{i+1}^{n-1} - \sigma_{i-1} \phi_{i-1}^{n-1} \right) + S_i^n, \end{aligned} \tag{4.8}$$

This additional term contains an auxiliary variables (χ and ϕ), and a damping factor σ_i. For the evaluation of the time evolution of these auxiliary variables and further implementation of the PML region, see [64]

4.3 Acoustic Source implementation

In the case of room acoustic simulations, a source is treated as a time-varying pressure signal applied to the point/points on an FDTD grid [69, 70]. Such pressure signal or source function is usually implemented by three methods, characterized by [71] as *hard, soft, and transparent* in FDTD. Each of such source methods differs in respect of their benefits and drawbacks.

4.3.1 Hard source

The *hard source* is the most common technique to implement the source in FDTD. In this method, the pressure at the source position is directly determined by the excitation function without updating the equations for the acoustic medium. Hence, in Eq. 4.4, the source term is dropped and treated as a time-varying Dirichlet boundary condition. Consequently, the update equation does not apply to this source node. For example, in one dimension, the update equations are:

$$p_i^n = -p_i^{n-2} + 2p_i^{n-1} + \frac{\Delta t^2}{\Delta x^2} c_i^2 (p_{i-1}^{n-1} - 2p_i^{n-1} + p_{i+1}^{n-1}) \tag{4.9}$$

$$p_{i,s}^n = S_n \tag{4.10}$$

Here, i_s is the source index position, $x_s = i_s \Delta x$ is the source position, $S_n = S(n\Delta t)$ and Δx,Δt being the spatial and temporal step size respectively.

It is evident from the above equation that the laws of mass and momentum conservation are not satisfied at the source node, which means the *hard source* does not comply with a superposition constraint. The source node is not affected by the surrounding nodes. In other words, *hard source* acts as a scattering node for every incoming wave and may cause unwanted low-frequency artifacts.

4.3.2 Soft source

The source-scattering can be overcome by employing *soft sources* where the excitation function is superimposed on the pressure at the source node. The soft method injects the driving function S_n directly into the update equation of the source point.

$$p_i^n = -p_i^{n-2} + 2p_i^{n-1} + \frac{\Delta t^2}{\Delta x^2} c_i^2 (p_{i-1}^{n-1} - 2p_i^{n-1} + p_{i+1}^{n-1}) + S_n \tag{4.11}$$

The problem with the soft method is that the intensity at the source point differs from the amplitude of the driving function (and the one of the hard method). Therefore, it must be normalized to obtain the correct value. The normalization factor is known for a few particular cases because it relies on acoustic pressure measurements at the source grid point. Still, for complex sources, it is difficult to estimate because of the directivity pattern the signal may have.

4.3.3 Transparent source

Transparent sources propagates signal same as of *hard source* but it is transparent to incident wave, hence the signal can not scatter. In particular, *transparent source* is regarded as the best means of determining the response of the system to a predefined excitation without suffering from numerical artifacts. This method requires the adjustment of the grid's impulse response, which is measured in advance of the simulation. We get this impulse by imposing a *hard source* model at the source location with Kronecker-δ as the driving function. The purpose is to evaluate the grid impulse response function at the source point. The *transparent source* model is obtained from the soft source model by subtracting the convolution of the grid impulse response I and the driving function S from the source node:

$$p_i^n = -p_i^{n-2} + 2p_i^{n-1} + \frac{\Delta t^2}{\Delta x^2} c_i^2 (p_{i-1}^{n-1} - 2p_i^{n-1} + p_{i+1}^{n-1}) + S_n - \sum_{m=1}^{n} I^{n-m+1} S^m \tag{4.12}$$

However, a transparent source implementation requires a very large computational domain to prevent reflections from the boundaries from interfering with the source node. It is, therefore, rather impractical due to the long calculation time required.

In this work, acoustic simulations are evaluated by incorporating such sources based on the specific conditions of the problem at hand.

4.4 Acoustic propagation in air layer/bubbly layer

The acoustic propagation entails the transfer of energy as the wave travels through the medium. This energy transfer is affected by many factors, i.e., the medium's density and temperature, the source wave frequency, and the presence of layers within the medium. Sound propagation in an air-water mixture layer is complex due to the stark difference in the densities and speed of sound of air and water. This difference leads to refraction and reflection in the mixture medium. Hence, we present an acoustic model that considers the layer's properties and considers different frequencies to predict the behavior of sound waves in homogeneous (all water) and heterogeneous (air-water mixture) media.

4.4.1 Acoustic source

Acoustic sources have an important role in noise prediction analysis. Several acoustic sources exist in underwater applications, i.e., pile driving, seismic airguns, and shipping. The sound power radiated by most of them can be modeled as a monopole, dipole, and quadruple a blend of them. These three types of sources are appropriate for the underwater noise problem as they represent archetypal models of real noise sources present at sea, i.e., ship propellers (tonal noise) and hydrokinetic turbines.

In this work, the sound source is considered and modeled as a monopole (point source).

4.4.1.1 Monopole source

Theoretically, the simplest source is a pulsating sphere that expands and contracts radially. If the radius r of the sphere is much smaller than the wavelength $kr << 1$, the source becomes a point source called *Monopole source* that emits sound waves uniformly in all directions [72]. The sound pressure field generated by the monopole is given by

$$P(r,t) = \frac{-\iota k \rho c Q_m}{4\pi r} e^{\iota(\omega t - kr)} \tag{4.13}$$

with r the distance from the monopole, t the time, Q_m the strength of the monopole, $\omega = 2\pi\nu$ the angular frequency, $k = 2\pi/\lambda$ the wavenumber and $c = \omega/k$ the speed of sound in the domain. It is pertinent to mention here that as we are interested in the low-frequency range, the frequency ν is chosen to be between 1 to 1000 Hz. The outcome of the pressure variations is calculated using a decibel scale, which is a measure of sound pressure level (SPL). Typically, SPL refers to the intensity of acoustic waves and is defined as

$$SPL = 20log_{10}\frac{p_{rms}}{p_0} \tag{4.14}$$

where p_{rms} is the root mean square of pressure and p_0 is the reference pressure which usually is 10^{-6} Pa in underwater surroundings.

4.4.2 Acoustic domain configuration

To model the domain of the problem in this study, the dimension of the propagation domain equals the real domain plus the presence of the PML layer necessary to impose the acoustic open-boundary conditions. Within the acoustic domain, the upper wall is a perfectly reflecting surface. This surface can mimic the presence of a very dense material compared to water, ensuring that all the acoustic waves reaching the boundary are reflected in phase. This is obtained by imposing a homogeneous Neumann boundary condition. The same above configuration for the acoustic domain is utilized for all the cases presented in this work. The monopole source is utilized; however, its implementation and positioning are different for each problem in this work.

4.5 Validation case: Acoustic propagation in a three-layered medium

Here, the acoustic model is tested without considering the development and dynamics of the air/water mixed phase. A simplified acoustic domain is considered, with a layer of pure air thickness of λ. This test case is necessary to become familiar with the problem and to be able to easily vary some parameters, such as the thickness of the air layer.

4.5.1 Acoustic domain of the validation case

The domain consists of a rectangular box measuring $1 \times 0.5 \times 1$ meters, as depicted in figure (4.1) Along the vertical axis, three layers are considered: the first, 0.03

meters thick and in contact with the upper part, consists of pure air; the second layer, 0.1 meters thick, consists of a mixture of air and water; the third layer, 0.87 meters thick, consists of pure water. The introduction of the mixture layer was necessary for numerical stability reasons, and in fact, this condition is more representative of the real case. By defining these three layers, we are able to derive the sound velocity along the vertical direction using the Wood equation as described in chapter 2. Figure (4.2) shows the density and sound velocity profiles along the vertical direction.

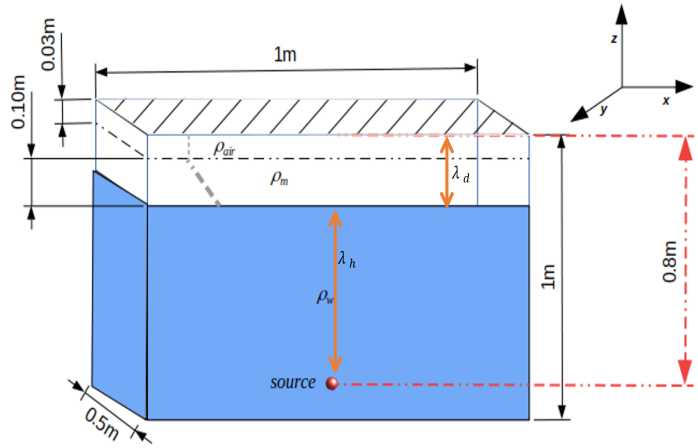

Figure 4.1: Schematic of acoustic domain with three layers (air, mixture, water) used in test case

The physical domain is discretized utilizing cubic cells of dimension equal to 0.005 with mumber of cells in x, y, z directions are $200 \times 100 \times 200$ respectively. Once the dimensions and properties of the domain have been defined, the monopole source is situated at the midpoint of the lateral sides (x and y) at ($0.5m$ and $0.25m$) respectively and positioned $0.8m$ away from the wall. The hard source injection technique is implemented in this case.

At this point, six simulations were performed by varying the source frequency. In particular, the frequencies used are: $1, 10, 100, 500, 1000, 5000Hz$. The idea is to evaluate the decrease in acoustic pressure induced on the domain's top surface due to the air layer's effect. This pressure is then compared with the results obtained when the air layer is absent. The sound pressure is recorded on a microphone located on the wall, exactly vertical to the source to carry out the comparison.

In figure (4.3), we present the results in terms of Sound Pressure Level (SPL), considering the SPL signal in the heterogeneous case (with air and a mixture of

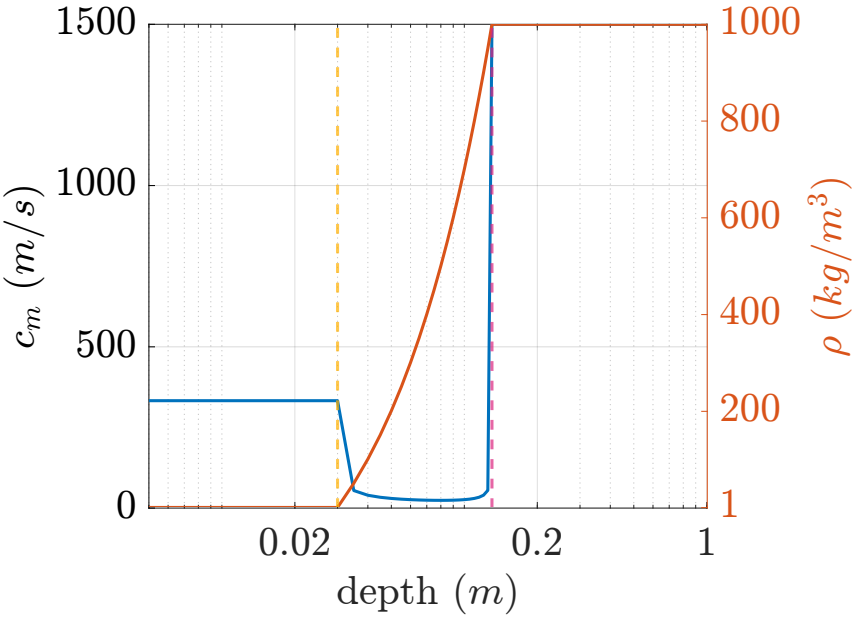

Figure 4.2: Vertical profiles of density (red) and sound velocity (blue) for the three-layer system with up to yellow dashed line: pure air, up to orange dashed line mixture of air water and out of the dashed lines all water

air and water) from which we subtract the SPL signal in the homogeneous case (all water). The x-axis is expressed in terms of $\lambda_{min} = c_{min}/\nu$, where c_{min} is the minimum sound velocity and ν is the frequency of the unidirectional source. It can be observed that signal attenuation is optimal for high frequencies while it is less effective for low frequencies. For the low-frequency range, i.e., 1 to 1000 Hz, It is found that the attenuation is between 30 to 45 dB.

This behavior is reasonable, and the trend of the graph is therefore appropriate except for a peak at $1000Hz$. This can be explained by noting that the minimum wavelength the signal assumes within the layer of air in this specific case is approximately 0.03, equal to the thickness of the air layer. It is, therefore, assumed that a phenomenon of trapping acoustic waves and resonance occurs within the air layer. In this case, a partial accumulation of energy within the air layer due to internal reflections can affect the attenuation capacity of the air layer at specific frequencies.

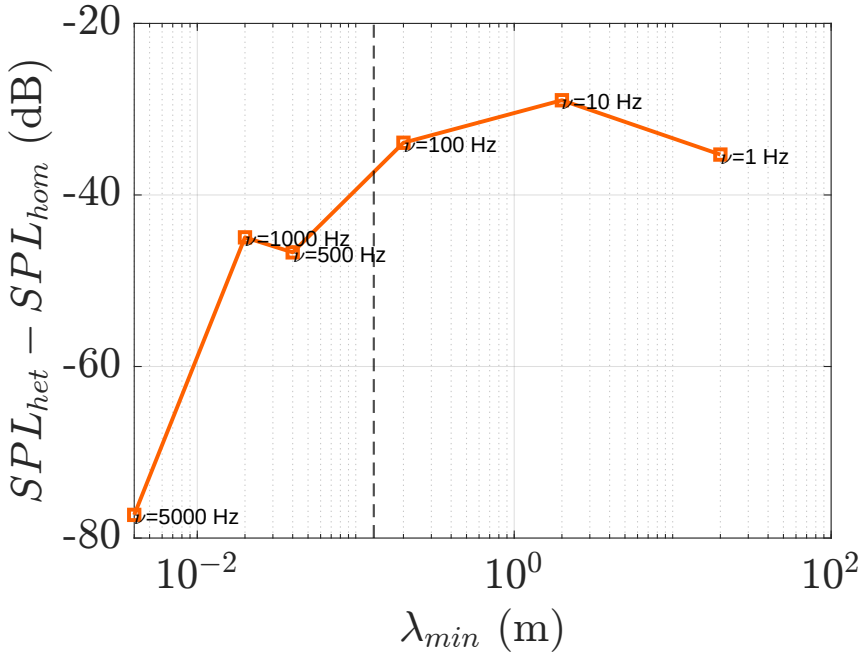

Figure 4.3: SPL attenuation for the case with air layer near the wall at source frequency of $1, 10, 100, 500, 1000$ and 5000. The dark vertical line in the graph indicates the thickness of the mixture layer, 0.1 m wide.

The above case serves as a preliminary overview to understand its functioning. The next chapters will consider the air-water mixture layer with realistic conditions (extracted from the CFD simulations) and provide detailed acoustic analysis.

Chapter 5

Acoustic Propagation in air-water mixture layer at LRN

This chapter evaluates the acoustic analysis of the layered media obtained from fluid dynamic simulation. As the CFD cases are presented in the chapter 3, now we will analyze the acoustic wave propagation in those two cases naming: the layer simulated at LRN and layers at HRN.

5.1 Acoustic domain

The acoustic experiment is conducted on the domain presented in Figure 5.1. The dimension of the propagation domain equals that of the fluid-dynamic numerical experiment plus the presence of the PML layer necessary to impose the acoustic open-boundary conditions. The physical domain is discretized utilizing cubic cells of dimension equal to 0.02 m, which are capable of correctly solving frequency up to 9.3 kHz. Within the acoustic domain, the upper wall is a perfectly reflecting surface. This surface can mimic the presence of a very dense material compared to water, ensuring that all the acoustic waves reaching the boundary are reflected in phase. This is obtained by imposing a homogeneous Neumann boundary condition.

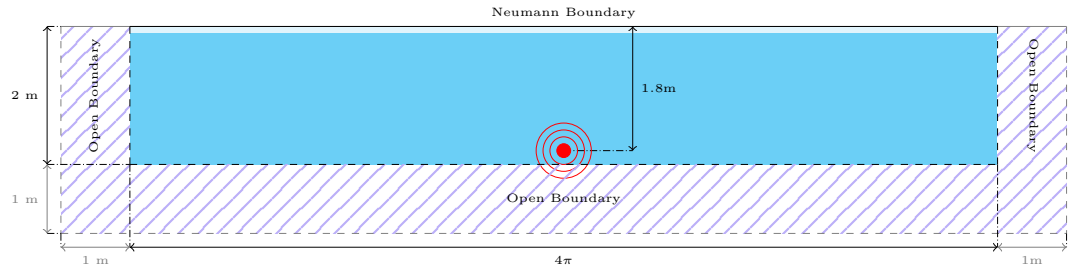

Figure 5.1: Schematic illustration of an acoustic domain.

The density ρ_m and the speed of sound c_m, derived from the α distribution,

are interpolated across the entire acoustic domain, considering both averaged and instantaneous fields. We utilize bilinear interpolation, which ensures the adaptation of the LES data available on a stretched grid to the acoustic domain characterized by a homogeneous space grid. Note that when defining the spatial distribution of ρ_m and c_m related to the instantaneous field, we needed to extend the lateral boundaries of the domain of 1 m. This was necessary to avoid artificial spurious reflection at the PML section. Indeed, this additional region dumps the density and the speed of sound linearly up to the constant values c_w and ρ_w. Linear smoothing of ρ_m and c_m is required only in the case of the instantaneous field because the PML is found to be sensitive to the non-uniform distribution of density and velocity along the horizontal direction. Indeed, when variable density and speed of sound occur along the $x - y$ plane, the damping of the acoustic waves is less effective. On the other hand, for uniform distribution, such as in layered media, the PML can absorb the acoustic waves with minimal reflection.

The *hard source* injection method is used to apply the acoustic source in the propagation domain. Specifically, a monopole source is generated by imposing the sinusoidal function at specific grid nodes: a square box of 4^3 nodes, thus having side $L = 0.08\,m$. A distributed (i.e., non-point-like) source imposed close to a reflecting surface may give rise to spurious reflections. We ensured that the implemented source met the recommended threshold discussed in [73]. Specifically, the Encumbrance non-dimensional number $EN = L^2/(\lambda D)$ is computed to assess the effectiveness of the *hard source* method. Here, L represents the width of the source, (λ) 150 m, 15 m and 1.5 m represents the characteristic wavelength of the source, and D =1.72 m represents the distance between the source and the reflecting surface. The EN number results to be $EN \leq 0.04$, which ensures that the spurious effects of using the hard source injection method close to a reflecting surface are negligible.

5.1.1 Data acquisition

The acoustic pattern analysis, presented and discussed in the following Section 5.2, is obtained by evaluating the Sound Pressure Level (SPL). The latter is defined as $SPL = 20\log_{10}(p_{rms}/p_0)$, where p_{rms} is the root mean square of the acoustic pressure and p_0 is the reference pressure in water (p_0 =10^{-6} Pa).

To compute the p_{rms}, the data has been collected starting at the time needed by an acoustic wave to reach the further boundary (considering in this calculation the speed of sound of the water). The time window considered for computing p_{rms} varies according to the source wavelength for computational reasons: we ensured that at least 10 periods were stored in case of the monopole source at 10 Hz; for higher

frequencies, we collected the signal for more than ~ 60 periods (in case of 100 Hz) and ~ 500 periods (in case of 1000 Hz).

5.2 Results and discussion

This section investigates how efficiently an air-water layer transmits sound when a single-frequency signal produced by a monopole source propagates into the layer across a range of frequencies. The results are evaluated in terms of Sound Pressure Level (SPL), and the efficiency is measured by comparing the signal recorded on a probe placed at the upper plate in the case of a pure water medium and in the presence of a layer of air-water mixture. As mentioned, the layer is reconstructed from the instantaneous field α, and the time-and-space averaged α field.

Hereafter, we refer to them as *Homogeneous case*, *Heterogeneous instantaneous case* and *Heterogeneous mean-field case*.

Three specific frequencies are selected: 10 Hz, 100 Hz and 1000 Hz. Future studies may extend the number of test cases, considering broad-band sources as well. We evaluate the acoustic energy distribution in space for each frequency. Then, we discuss the difference between them along a specific line connecting the source to the upper plate. This allows us to evaluate the air layer's absorption property.

The SPL contours for the ν =1000 Hz monopole are shown for the homogeneous medium, heterogeneous mean, and instantaneous fields in Figure 5.2. In the homogenous scenario (Fig.5.2a), a region of minimum SPL is observed; it is not parallel to the reflecting surface but bends on the source sides (blue spots). The presence of this region is explained by the classical Lloyd mirror interference theory. This occurs because the source's wavelength is comparable to the distance between the source and the reflecting surface; consequently, the reflected wave interferes with the incoming wave. An increase in acoustic pressure is observed on the upper wall, and it is consistent with the hypothesis of a perfectly reflected surface.

The existence of the air layer drastically alters the acoustic energy distribution in space. In Figure 5.2b, the mean profile of α is considered (the one depicted in the figure), and a clear reduction in acoustic pressure inside the air layer is observed, almost neglecting the waves incident to the layer. In the proximity of the source, a slight increase in acoustic pressure compared to the homogeneous case is observable. Moreover, a series of SPL minima along the line connecting the source to the wall arises. The minima's presence is still the result of Lloyd's mirror interference effects in conjunction with the variation of the speed of sound. As we move towards the reflecting surface, the speed of sound decreases (Fig.3.9), which affects the signal wavelength, which is drastically reduced. This short-wave signal

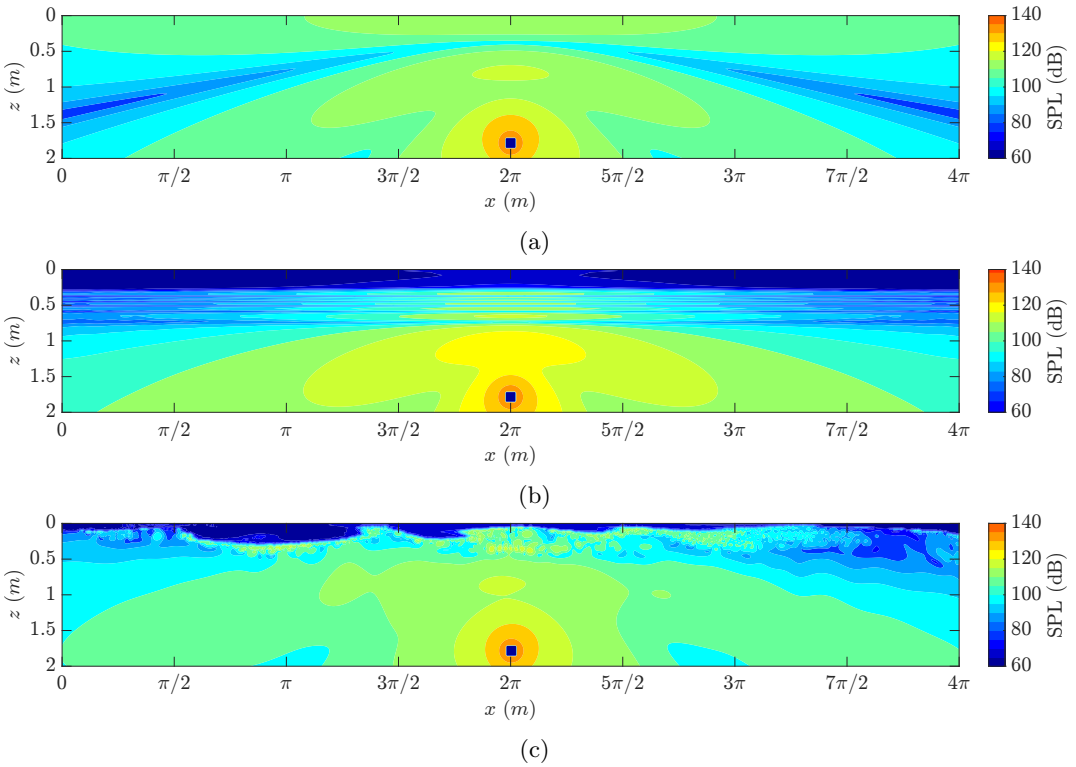

Figure 5.2: Contour of SPL on the x-z plane at $y = 2\pi/3$ for (a) Homogeneous field, (b) Heterogeneous mean-field, (c) Heterogeneous instantaneous field, excited by a monopole source with a ν =1000 Hz.

creates an interference pattern with multiple minima and maxima (see the top part of figure 5.2b). This is in contrast to the smooth pattern observed in the homogeneous case. The Lloyd's mirror effect is still observable since the air layer acts as a reflecting surface parallel to the upper wall. In this case, the air layer acts as a free surface. Results are those often observed when accounting for a sharp water-air interface in an underwater environment. This is not true for the instantaneous case (Fig.5.2c) since the non-uniform distribution of α generates a three-dimensional variation of the air layer (Fig. 3.5). As a result, the acoustic field is dominated by the scattering effects of the uneven distribution of the air layer. Although we still observe a reduction of acoustic pressure on the upper wall, it is not continuous across the horizontal direction of the domain, unlike in the heterogeneous mean case. We can observe spots of lower acoustic energy that resemble the α distribution in the x-z plane (Fig. 3.6a). Just below the mixture zone, peaks in SPL are observed, attributed to the constructive interaction of waves reflected by a non-smooth air distribution. This is most likely the combined effect of using a very high-frequency source and reducing

the speed of sound near the upper wall. This aspect enables the acoustic waves to be scattered by small variations of the air surface, which is less visible for the lower frequencies.

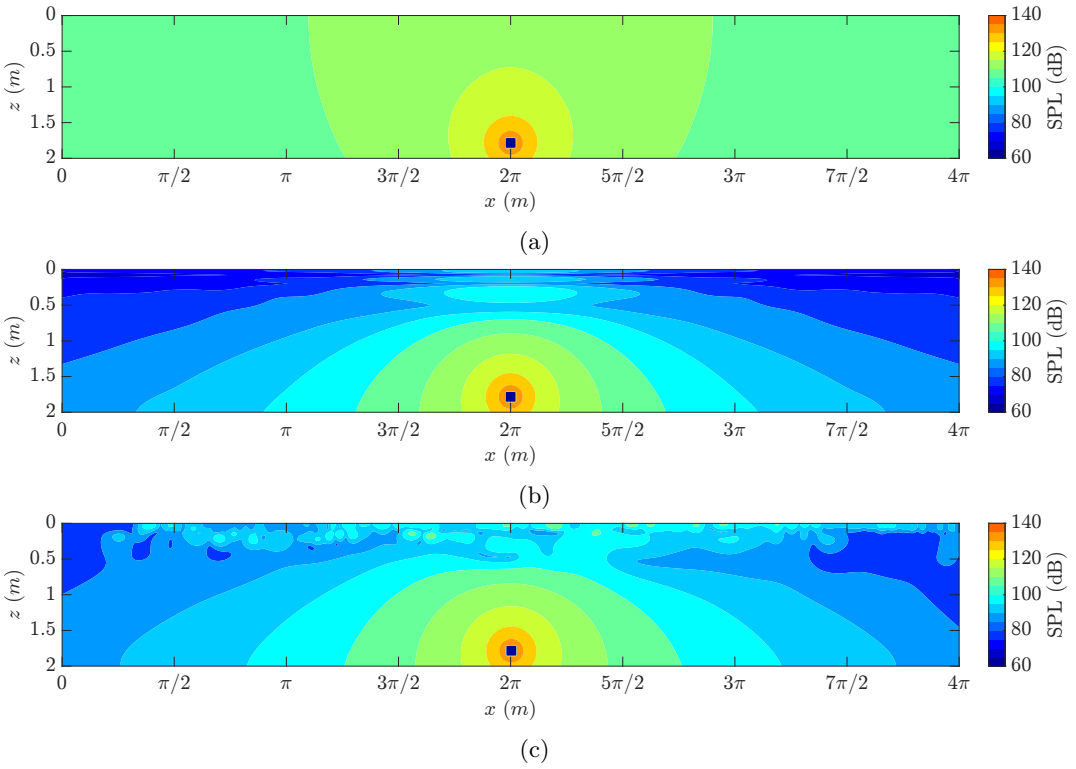

Figure 5.3: Contour of SPL on the x-z plane at $y = 2\pi/3$ for (a) Homogeneous field, (b) Heterogeneous mean-field, (c) Heterogeneous instantaneous field, excited by a monopole source with ν =100 Hz.

For both the 100 Hz and 10 Hz sources in the homogeneous case, the acoustic field (Fig.5.3a and Fig.5.4a) is found to be uniform, meaning that there are no regions of minimum SPL values due to Llyod mirror effect, as those observed in the 1000 Hz source. However, when we take into account the mean α field, we observe the presence of minima planes. Specifically, we observe multiple planes in the 100 Hz case (Fig.5.3b), and a single plane in the 10 Hz case, (Fig.5.4b).

For both frequencies (100 Hz and 10 Hz) in the heterogenous mean case, the acoustic waves are partially able to reach the surface and are not entirely reflected by the air layer. This results in increased acoustic energy transmitted to the wall despite the presence of the air. Note that the largest transmission of the signal is limited to the zone directly above the acoustic source. At the same time, a reduction in noise level with respect to the homogeneous case is still observed at the domain

sides. This means that when the incident angles to the horizontal air layer differ from approximately $\sim 90°$, most of the acoustic waves are still reflected and cannot reach the surface.

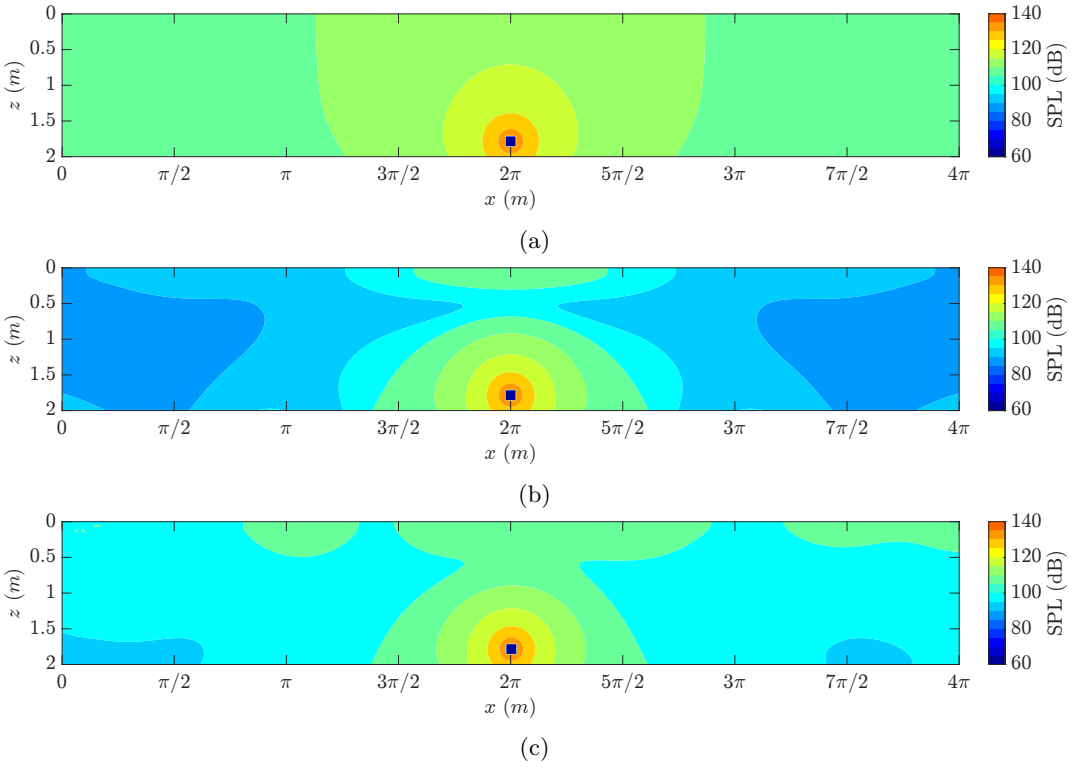

Figure 5.4: Contour of SPL on the x-z plane at $y = 2\pi/3$ for (a) Homogeneous field, (b) Heterogeneous mean field, (c) Heterogeneous instantaneous field, excited by a monopole source with ν =10 Hz.

A major difference between the 100 Hz and 10 Hz frequencies arises when the heterogeneous instantaneous case is considered (Fig.5.3c and Fig.5.4c). For the 100 Hz source, we observe spots of higher value of acoustic energy similar to those pointed out in the 1000 Hz case, but a clear absorption of the acoustic energy in the air layer is not visible. Thus, at this frequency, so as for lower ones, the air layer tends to become ineffective. However, the presence of a mixture region in $0 < z < 0.5$, where spots occur, seems to trap acoustic energy at this frequency. Note that the wavelength of the signal at $\nu_{100} = 100\,Hz$ becomes $\lambda_{min} = c_{min}/\nu_{100} \sim 0.2\,m$ when considering the minimum sound speed reached in the mixture region. This wavelength is comparable to the layer thickness, thus resonance effects may come into play. Lowering the source frequency at $\nu = 10\,Hz$ and considering the instantaneous distribution of α (Fig.5.4c), spots disappear, and most of the energy is transmitted

to the upper plate.

To summarize, the air and mixture layer is most effective for high-frequency sources. In addition, considering a uniform layer of air and/or air-water mixture may not be representative of the effectiveness of a layer that adjusts itself on a plate according to the flow and specific conditions. Particularly, the uniform layer, represented in our case by the heterogeneous mean-field results, acts as a much more effective acoustic barrier compared to what occurs in the case of instantaneous (non-uniform) fields.

5.2.1 Quantitative analysis of the thick air layer

A quantitative analysis of the acoustic pressure is conducted by extracting the SPL along a line, orthogonal to the upper plate, connecting the source to the wall, for the three different cases (Fig.5.5) and evaluating the SPL on a microphone located on the upper wall.

In Fig.5.5a, data are extracted in the homogeneous case for the sake of comparison. As expected, the same value of SPL at the wall (117 dB) is obtained when considering different source frequencies: the minimal difference (≤ 0.3 dB) in the SPL between the three frequencies at the wall can be attributed to the implementation of the source, which is sensitive to injecting sources with increasing frequency. At a frequency of 1000 Hz, local minima occur due to acoustic patterns typical in the presence of reflective boundaries. These minima are clearly visible in the contour plot of Fig. 5.2a.

The profiles for the non-homogeneous cases (Fig. 5.5b and 5.5c) show the differences observed in the contour plots. In particular, all the signals are lowered, meaning that even for long wavelengths, the layer acts as a sound barrier. Also, the local minima resulting from Lloyd's mirror interference, before mentioned, are visible in the case of the source at $100\,Hz$ and $1000\,Hz$. Note that for the $1000\,Hz$ case, it is evident that they occur below the mixture region at $z > 0.3$.

In the heterogeneous instantaneous case, both the signals for $100\,Hz$ and $10\,Hz$ behave somehow similarly with respect to the mean field distribution. We can assert that the lower the frequencies of the incident wave signal, the more the layer is perceived in the same way, whether it is averaged or not, meaning that longer wavelengths do not perceive the mixture distribution. While, as reasonable, the local variation of α can significantly influence signals with high frequencies since the reflections occur with respect to *structures* (namely the spot of air or air-water mixture), which have a scale length comparable to the wavelength. We note that in the case of the source at $1000\,Hz$, the profile is almost flat close to the source, and then, after an abrupt increase, a sharp decrease occurs near the wall. This is due to

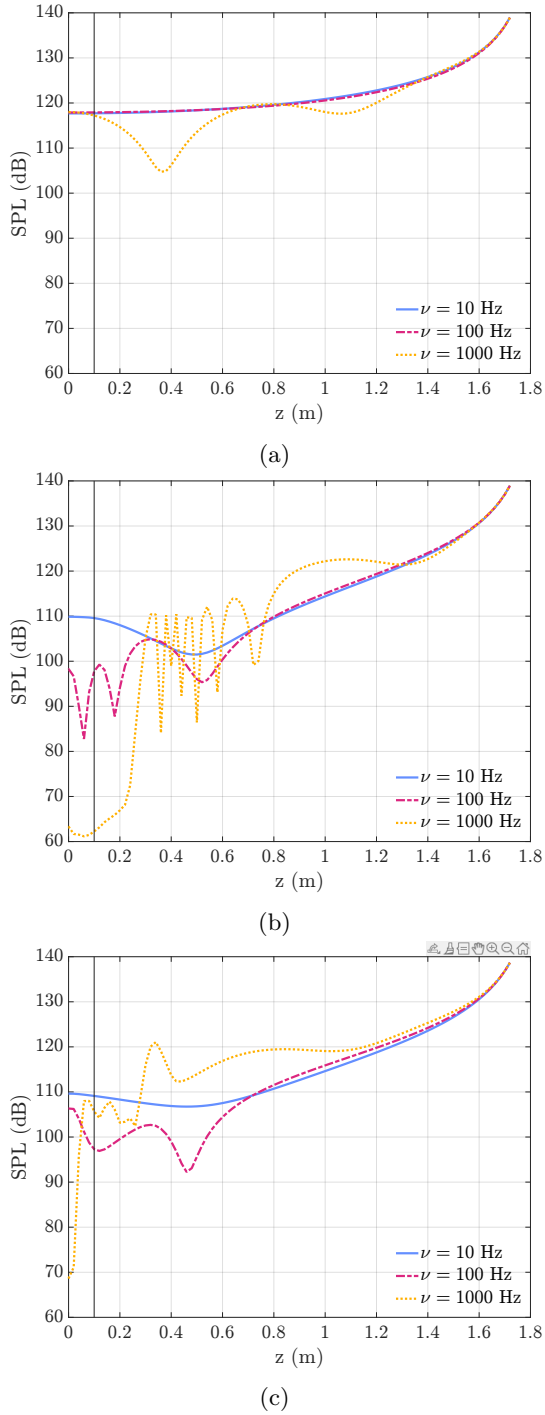

Figure 5.5: SPL along the z direction at $(x = 2\pi, y = 2\pi/3)$ for (a) Homogeneous field, (b) Heterogeneous mean-field, (c) Heterogeneous instantaneous field, excited by a monopole source with $\nu = 10\,\text{Hz}$, $100\,\text{Hz}$ and $1000\,\text{Hz}$. The black line at x =0.1 m represents the air injection width.

the spot distribution of acoustic pressure in the domain as discussed previously in Fig.5.2c, and other lines selected would give a different result.

5.2.2 Efficacy of the thick air layer

Finally, we quantify in 6.5 the effectiveness of the absorbing layer, evaluating the SPL value at the wall. Specifically, the probe is positioned on the upper boundary directly above the source, and we report in the figure the difference in dB obtained with respect to the homogeneous case.

For the heterogeneous mean case, the SPL at the wall is lowered up to 63.3 dB, 96.7 dB and 109.9 dB for 1000 Hz, 100 Hz and 10 Hz, respectively. While in the instantaneous case, the SPL values measured at the wall are 68.6 dB, 106.3 dB and 109.6 dB for 1000 Hz, 100 Hz and 10 Hz, respectively.

The x-axis is expressed in terms of $\lambda_{min} = c_{min}/\nu$ with c_{min} minimum sound speed calculated with the Wood's formula (Eq.3.1) and ν frequency of the monopole source. This choice clearly shows that only the wavelength associated with the highest frequency (1000 Hz) is shorter than the length scale of the layer. Also, as observed before, the λ_{min} in the case of the mid-frequency 100 Hz is comparable to the layer thickness. This aspect is important for explaining possible resonance effects.

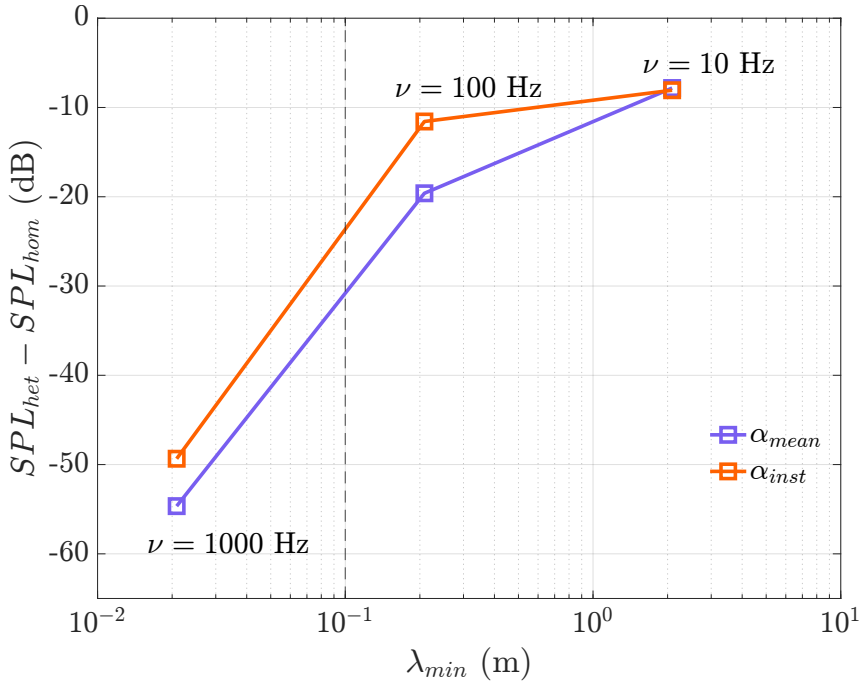

Figure 5.6: SPL attenuation for the Instantaneous field and mean fields near a wall, at source frequencies of 10 Hz, 100 Hz and 1000 Hz The dashed vertical line indicates the thickness of the mixture layer, 0.1 m wide.

The results show that increasing the frequency of the source increases the absorption

property of the thin layer for both cases (mean and instantaneous); however, there is an apparent increase in the layer's efficiency when the wavelength is shorter than the dimension of the mixture layer. Namely, the measure of efficiency is not linear with respect to the source wavelength.

Considering the α distribution, we observe that the signal at the lowest frequency (10 Hz) is almost insensible to the spatial variation of the air content. Conversely, a clear difference is observed for the two higher frequencies (100 Hz and 1000 Hz); the instantaneous mean distribution is ~ 5 dB to 8 dB less efficient in reducing the acoustic waves, or, to say in another way, hypothesizing a flat and uniform absorbing layer overestimates the sound absorbing efficiency.

Chapter 6

Acoustic Propagation in air-water mixture layers at HRN

In this chapter, we present the acoustic analysis of the thin air layer formed in the high Reynolds case using the WMLES approach. The acoustic domain and methodology differ from the previous case due to the reduced size of the propagation domain. However, the main goal is to compare the results with those of the low Reynolds number case. The numerical experiments involve three cases with varying air layer thickness and the amount of air injected into the domain, as discussed in Chapter 3. Hence, we performed three acoustic simulations for each layer: the first with the thickness equal to $\lambda_{a1} = 0.0022$ and the second $\lambda_{a2} = 0.0044$, both injecting the pure air ($\alpha = 1$) in the fluid domain and third with the layer of thickness equal to $\lambda_{a1} = 0.0022$ injecting a mixture of air and water ($< \alpha = 0.5$).

6.1 Acoustic domain

The high Reynolds number case acoustic experiment is carried out on the domain presented in Figure 6.7. The dimension of the propagation domain equals that of the fluid-dynamic simulation using WMLES, i.e., $0.1 \times 0.1 \times 0.02$ m plus the presence of the PML layer necessary to impose the acoustic open-boundary conditions. The physical domain is discretized by utilizing cubic cells of dimension equal to 0.0004 m. The top wall is a perfectly reflecting surface as in the former cases and obtained by imposing a homogeneous Neumann boundary condition.

The way we handle the acoustic source for the high Reynolds number case is differs from the low Reynolds number case. Because the domain size is smaller compared to the previous case, we carried out the acoustic simulations by placing the source outside the domain. This was done to make the results comparable with the low Reynolds number case. Having the source inside the domain would have been impractical due to the associated computational costs of the bigger propagation domain. The

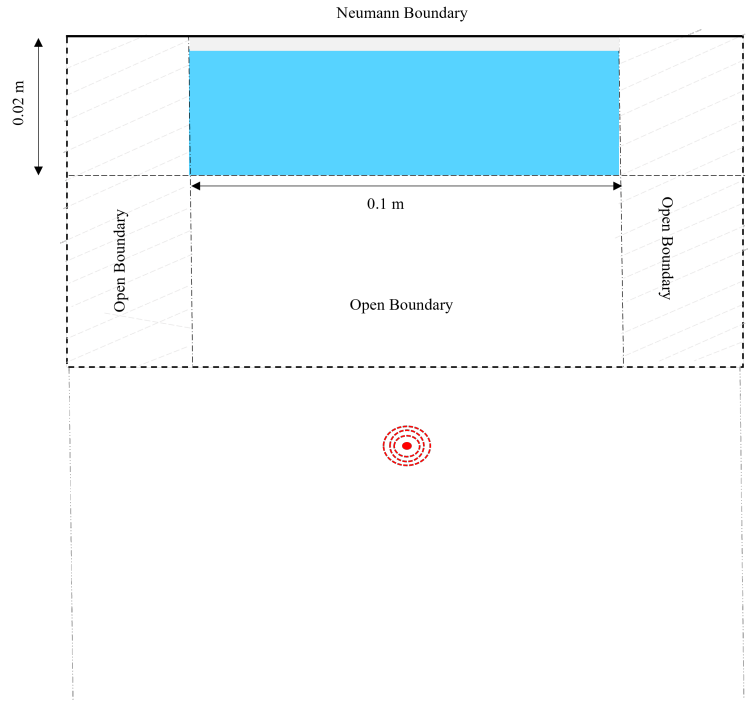

Figure 6.1: Schematic illustration of a section normal to the flat plate of the acoustic domain for the high Reynolds number case.

acoustic pressure generated by the outside source excites a plane perpendicular to the flat plate inside the domain. Therefore, the acoustic pressure generated by a monopole source at 2 meter computed by the analytical function is imposed using the *soft source* injection method inside the domain since the *hard source* method is not applicable in this case. Indeed, a Dirichlet boundary condition applied to the whole plane scatters all the waves reflected by the flat plate and the air layer. The soft source method avoids this problem since it enables the reflected acoustic waves to pass. Moreover, in this case, we only considered the averaged fields of α distribution and then calculated the density ρ_m and the speed of sound c_m. As mentioned in the previous case, these are interpolated across the entire acoustic domain. The method to collect the microphones is the same as in the previous case. See section 5.1.1. Two cases are considered for the three configurations of the air layer: a homogeneous medium (all water domain) and the mixture medium ρ_m obtained from the fluid dynamic simulations. The data are collected for a minimum of 6 periods of each frequency considered in the acoustic experiment.

6.2 Result and Discussion: Acoustic analysis in variable layers

In this section, the acoustic results obtained by propagating a signal within two air-water mixture layer thicknesses, denoted as $\lambda_{a1} = 0.0022$ and $\lambda_{a2} = 0.0044$ that are simulated using WMLES are discussed.

The acoustic response of the air layer is tested with a monochromatic monopole source generating acoustic pressure in the low-frequency range 40 to 1000 Hz. For the visualization, the contours of 1000 Hz, 120 Hz and 40 Hz are considered. The acoustic energy distribution in space is evaluated, and the difference between them by considering a specific point of the upper plate for frequency 1000 Hz, 40 Hz, 200 Hz, 120 Hz, 80 Hz and 40 Hz is also investigated.

To visualize the propagation in space, the contours of three frequencies, $1000Hz$, $120Hz$, and $40Hz$, are shown for a) homogeneous domain, b) Heterogeneous domain with air layer $\lambda_{a1} = 0.0022$ and c)Heterogeneous domain with air layer $\lambda_{a2} = 0.0044$.

Figure 6.2 shows the visualization of a monopole source of frequency 1000 Hz. In figure 6.2a, the uniform acoustic pressure variation is observed along a wall. However, some symmetrical patterns of decreasing SPLs on either side are also observed. This may be due to the consequences of a narrow domain. For the heterogeneous case with $\lambda_{a1} = 0.0022m$ in figure 6.2b, the mitigation of SPL inside the layer is observed. However, the minimum pressure is noted on the edges of the domain, and a slightly augmented pressure level in the center is also observed within the layer. Overall, in comparison to homogeneous cases, a reduction in pressure is observed. Similarly, in figure 6.2c, the same minimum SPLs are found around the edges when the air layer is doubled. However, pronounced attenuation is observed in air layer $\lambda_{a2} = 0.0044m$.

In figure 6.3a, the same behavior is observed as we visualize for 1000Hz. For the heterogeneous case with $\lambda_{a1} = 0.0022m$ in figure 6.3b, the increasing SPLs are found within the layer. Visualizing and differentiating the pressure levels is difficult as they vary with such small values, i.e., 0.5 db. However, in comparison to the homogeneous case, a reduction in pressure is observed. In figure 6.3c, when the air layer is doubled, the pressure value is reduced, and more attenuation is observed than in the case of the air layer $\lambda_{a1} = 0.0022m$.

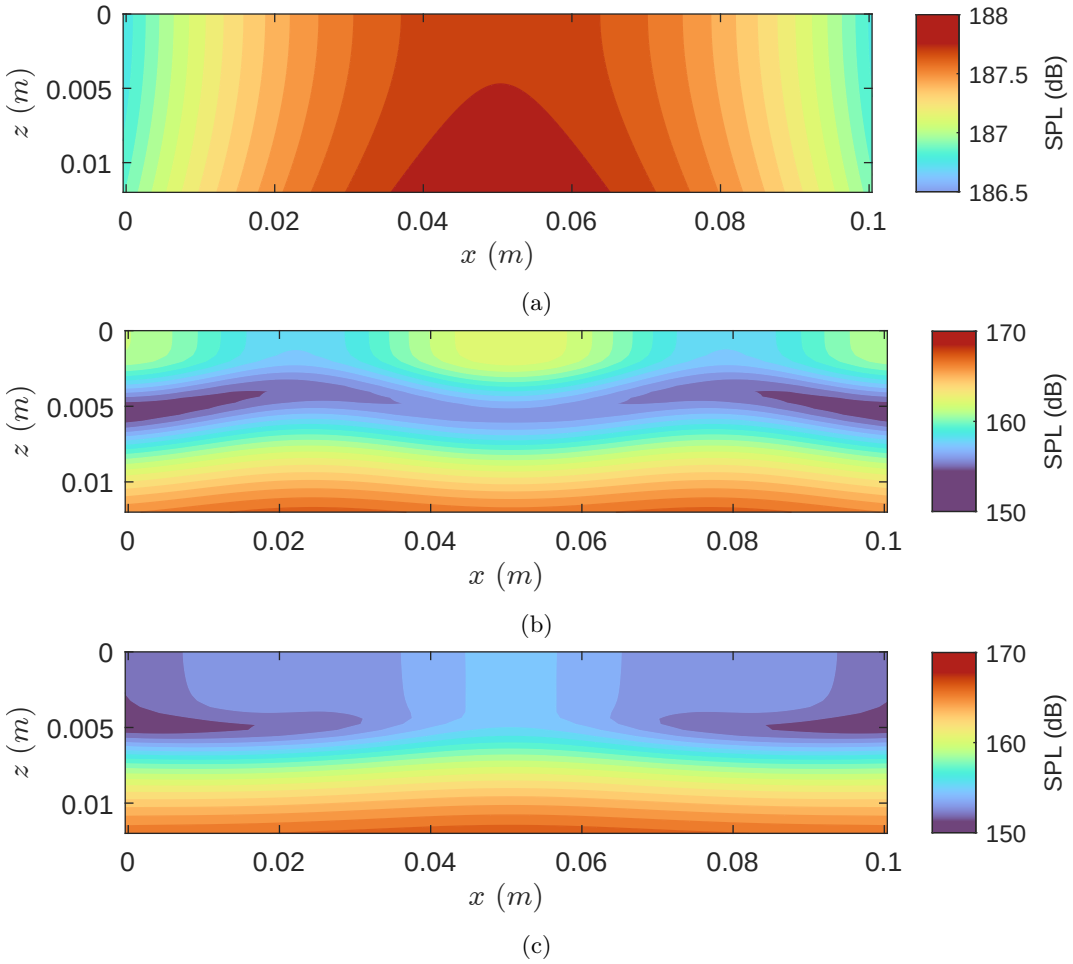

Figure 6.2: Contour of SPL on the x-z plane at $y = 0.05$ for (a) Homogeneous field, (b) Heterogeneous mean field: $\lambda_{a1} = 0.0022$ (c)$\lambda_{a2} = 0.0044$ excited by a monopole source with ν =1000 Hz.

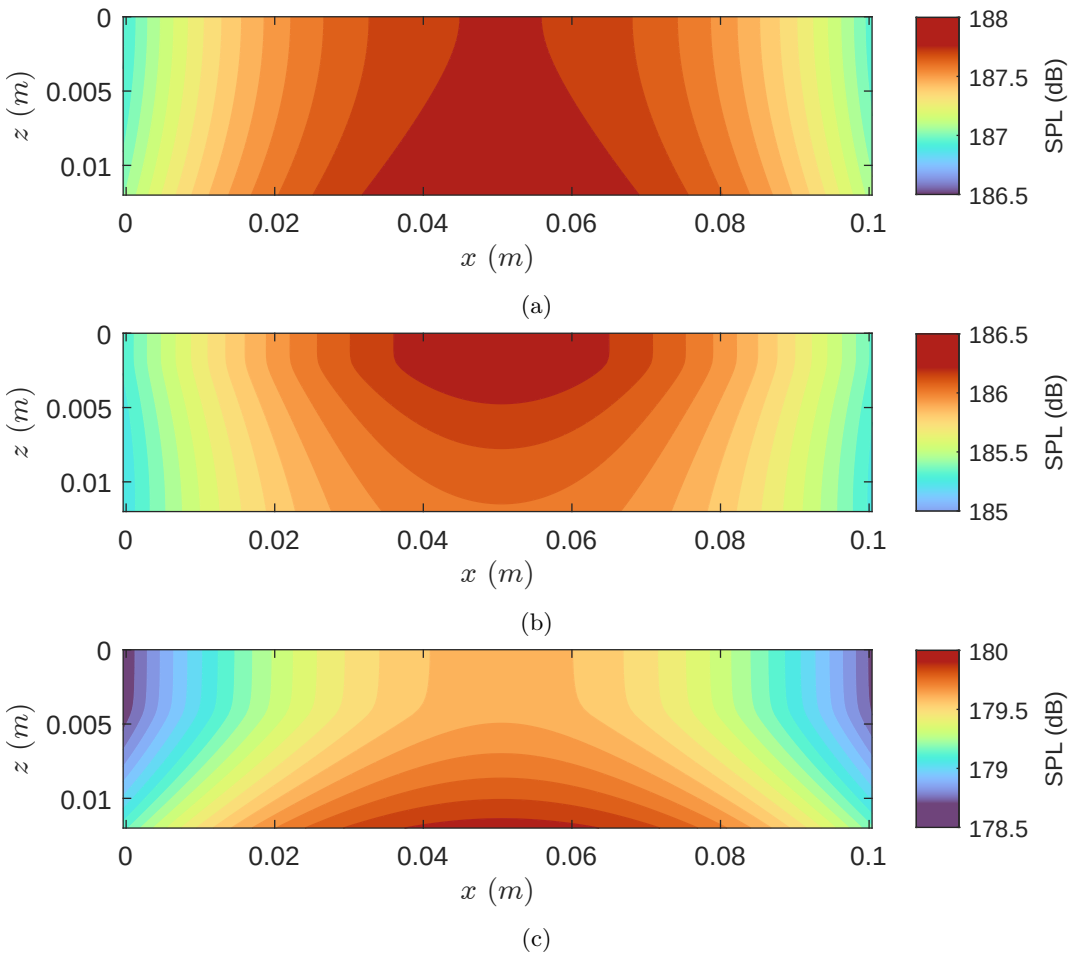

Figure 6.3: Contour of SPL on the x-z plane at $y = 0.05$ for (a) Homogeneous field, (b) Heterogeneous mean field: $\lambda_{a1} = 0.0022$ (c)$\lambda_{a2} = 0.0044$ excited by a monopole source with ν =120 Hz.

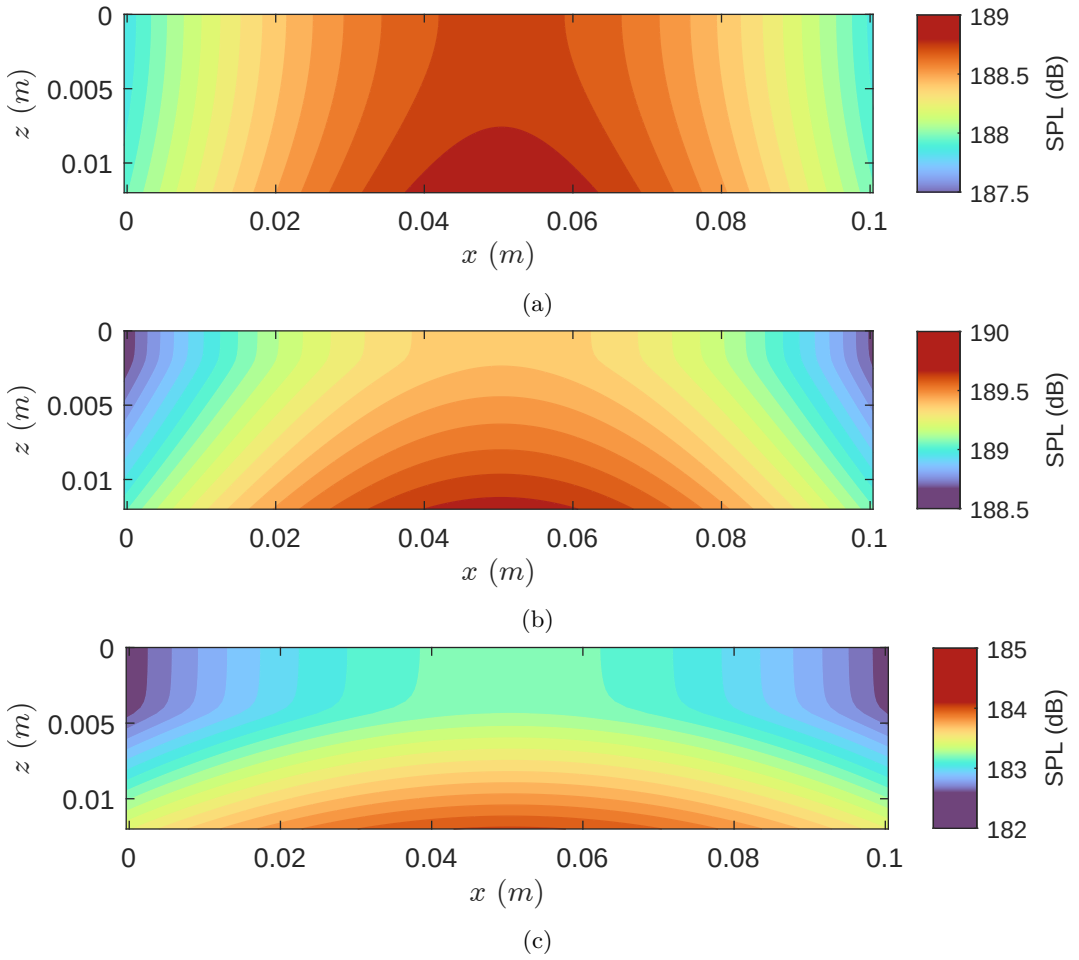

Figure 6.4: Contour of SPL on the x-z plane at $y = 0.05$ for (a) Homogeneous field, (b) Heterogeneous mean field: $\lambda_{a1} = 0.0022$ (c)$\lambda_{a2} = 0.0044$ excited by a monopole source with ν =40 Hz.

For the signal of $40Hz$, inhomogeneous domain 6.4a , the propagation is observed to be similar as to $1000Hz$. For the heterogeneous case, the attenuation is observed inside the layer of λ_{a1}(unlike the signal with ν_{120}). The attenuation is larger in λ_{a2} case that is consistent with the preceding signals.

6.2.1 Efficacy of the thin air layers in 3D domain

In order to assess the absorption of noise in both the air layers, we evaluated the SPL value at the wall as calculated in the previous cases. In figure 6.5, the comparison of mitigation in SPL by varying the thickness of the air layer is shown. For the thickness of λ_{a1}, the pressure value is lowered up to 24.83 dB, 3.4 dB, 2.6 dB and 1.4 dB for 1000 Hz, 240 Hz, 200 Hz and 120 Hz. However, for the lowest frequencies 80 Hz and 40 Hz, no such attenuation is observed. In the air layer of λ_{a2}, the reduction in SPL is more pronounced than in the λ_{a1}. The reduction is upto 32.9 dB, 11 dB, 10 dB, 8 dB, 6.4 dB and 5.5 dB for 1000 Hz, 240 Hz, 200 Hz, 120 Hz, 80 Hz and 40 Hz. Hence, we can say that the air barrier with more thickness is more efficient in attenuating the noise.

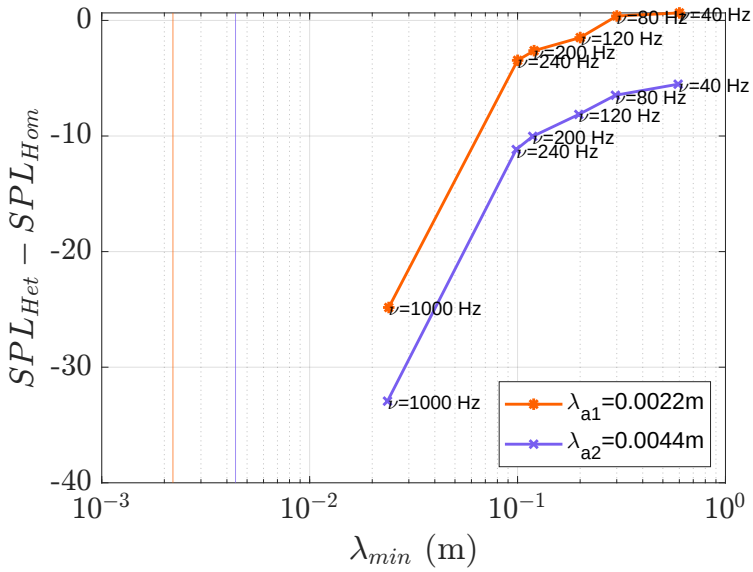

Figure 6.5: SPL attenuation for mean fields in an air layer:λ_{a1} and λ_{a2} near a wall, at source frequencies of 40 Hz, 80 Hz, 120 Hz, 200 Hz, 240 Hz and 1000 Hz The dashed vertical lines indicates the thicknesses of the mixture layers, 0.0022 m and 0.0044 m wide.

6.3 Result and Discussion: Acoustic analysis in air layer of thickness (λ_{a_1}) considering $(0.5 < \alpha < 1)$

We also try to perform acoustic propagation by considering the air layer that starts with the mixture but not with pure air. The same frequency range of source is chosen for the propagation in the domain. Figure 6.6 demonstrates that this mixture kind of air layer has no attenuation effect except for the signal with 1000 Hz.

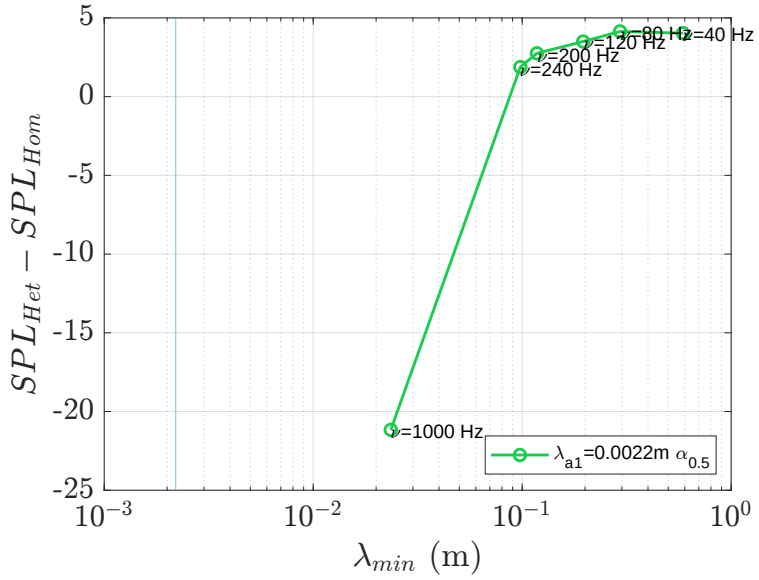

Figure 6.6: SPL attenuation for mean fields in an air layer:λ_{a1} with $(0.5 < \alpha < 1)$ near a wall, at source frequencies of 40 Hz, 80 Hz, 120 Hz, 200 Hz, 240 Hz and 1000 Hz The dashed vertical lines indicates the thickness of the mixture layer, 0.0022 m wide.

Overall, in these three cases, the order of attenuation is not substantial compared to the previous case of an air layer of 0.1m simulated by LES. This is due to the fact that the source is positioned very far from the wall. In fact, the air layer is of the order of 0.002 meters, while the source is positioned 2 m away from the wall. Moreover, the sound source is taken as the soft source and implemented in an unusual way, which makes it difficult to consider a 3D domain that is large enough to include the source and resolution to appropriately capture the propagation of a wave in this layer of air. Hence, to streamline the acoustic analysis, it is necessary to simplify the process by conducting a 1D acoustic simulation using the 1D mean distribution of air layers.

6.4 1D simulation

Another method to study the sound waves produced by a single-frequency sound source is to analyze them in a one-dimensional space without taking into account the geometrical spreading of the sound waves. This method can provide initial insights into how the air absorbs the sound. The sound source is introduced using the transparent source method, which emits the same signal as a hard source but without scattering the incoming wave. This method can only be used for single-point sources and, in some cases, for sources on a flat surface. The analysis is conducted similarly to the previous case by studying the sound pressure at a microphone placed above the flat surface. In this scenario, the sound propagates only along a line perpendicular to the flat surface, connecting the source to the microphone.

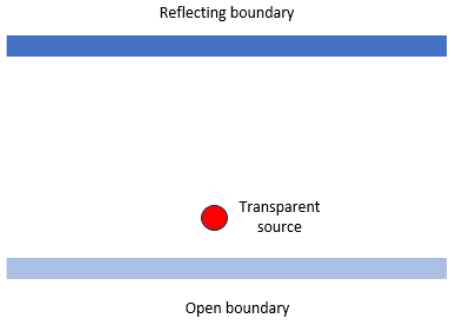

Figure 6.7: Schematic illustration of an acoustic 1D domain.

The propagating wave encountered a variation in density and speed of sound dictated by the average profile of α, as represented earlier for the high Reynolds number case. The solution of the wave equation in a 1D domain allowed the use of the transparent method, which made the source transparent to all reflected waves. In this way, the reflections that occur at the mixture-water interface do not alter the imposed source and hence improve the reliability of the results as shown in figure 6.8.

6.4.1 Efficacy of the air layers in 1D domain

The reduction of acoustic pressure level can be clearly seen in the case with layer starting from the mixed air $\alpha_{0.5}$, presented in the green line. The reduction ranges from 32 dB to 5 dB as we approach the lowest frequency. In the case of pure air with the thickness λ_{a1}, the attenuation is more pronounced and approximately differs by 10 from the case of mixed air. Furthermore, with the thickness λ_{a2}, the SPL difference

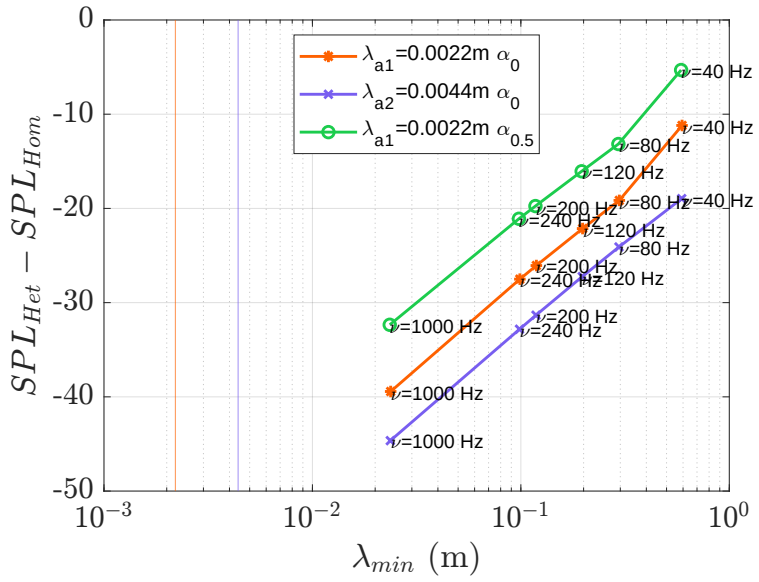

Figure 6.8: SPL attenuation for mean fields of all three air layers:λ_{a1} and λ_{a2} and λ_{a1} with $(0.5 < \alpha < 1)$ near a wall, at source frequencies of 40 Hz, 80 Hz, 120 Hz, 200 Hz, 240 Hz and 1000 Hz

is even more significant i.e., 45 dB for 1000 Hz and 18 dB for 40 Hz. However, this approach sacrifices the three-dimensionality of the acoustic wave.

The analysis shows a clear trend in both 3D and 1D analysis: increasing the width or thickness of the air layer significantly reduces noise. However, when only a fraction of air is injected (alpha = 0.5), the noise reduction is lower compared to using pure air. This is because the air layer has minimal variation in sound speed. Additionally, noise reduction varies with frequency in all three layers, following a trend similar to the previous case of a thick layer simulated through LES. Increasing the frequency of the source enhances the effectiveness of the air layer.

Chapter 7

Preliminary numerical investigation of a bubble collapse near a wall

The study of bubble barriers, particularly focusing on single bubble dynamics and bubble clouds, is essential for understanding and optimizing their effectiveness in various applications such as pollution control, sediment management, and noise reduction. In the previous chapters, we have studied the bubble barriers which which is uniformly distributed bubbles, imitate as a bubble cloud . This chapter shifts the focus to the behavior of individual bubbles, particularly how a single bubble near a wall can affect the surrounding environment. Hence, we report a preliminary study of a single bubble near a wall, including the time evolution of the temperature field, pressure field, and velocity field during the bubble's collapsing stage.

7.1 Characteristics of a bubble near a wall

Bubble dynamics is a very complex and important aspect in most environmental and ocean engineering application, as well as in hydraulics, and medical sciences. For example, cavitation is a crucial phenomenon in naval and hydraulic engineering ([74]). Cavitation is a common two-phase gas and liquid flow (or three-phase flow when also vapor phase is considered) that occurs when the flow pressure drops below the vapor pressure and the fluid changes from the liquid to the gas phase. In particular, cavitation often occurs in flows around propellers ([75]) and hydraulic pumps ([76]). Another example is the high-speed underwater jet that generates a cavitation bubble cloud that is transported by the fluid flow. As well known for the cavitation erosion problems [77], when the bubbles hit a solid surface, it is eroded due to the collapse of the bubbles. In addition, the study of bubble dynamics plays an important role in the field of environmental engineering for the reduction of acoustic noise pollution [78]. The theoretical study of bubble dynamics has come a long way as the first theory on the bubble dynamic was carried out by [79]. The author studied a spherical bubble

immersed in a quiescent fluid flow, with the hypothesis of a negligible viscosity of the fluid, the surface tension of the bubble was neglected and the internal pressure is constant. In addition, [80] extended the Besant analysis considering the internal pressure variation, using Boyle's law of gas. Finally, [81] individuated the well-known "Rayleigh-Plesset" (RP) equation, considering the spherical bubble in a quiescent viscous fluid. Later, Keller [82] formulated the "Keller–Kolodner" (KK) equation by considering the compressibility effects of the liquid. The RP and KK theoretical equations are commonly used to verify the experimental or numerical results.

7.1.1 Bubble collapse

Bubble collapse is crucial to understand because of the noise and material damage that can result from high velocities, pressures, and temperatures. The thermodynamical effects also play a significant role in the last stage of cavitation bubble collapse. As the liquid pours into the bubble, the material inside undergoes significant compression, generating extremely high temperatures. The rapid collapse, typically within microseconds, leads to the assumption of adiabatic behavior in the non-condensable gas of the bubble. The maximum temperature, calculated to be around 8800 K, remains a matter of debate due to inconclusive experimental results influenced by various environmental factors. The energetic behaviors are closely related to the generation of the pressure waves and the high-speed liquid jet during bubble collapse. The generation of bubbles and understanding the thermodynamic complexities near a rigid boundary remains challenging, even through theoretical or experimental means alone. However, numerical simulations, such as those conducted by Yuan et al. [83]. offer valuable insights into gas-liquid heat transfer and other complex dynamics. Numerous studies employing traditional numerical methods and computational fluid dynamics have further explored the thermodynamics of cavitation bubbles [84, 85, 86, 87, 88]. The recent study by [87] investigated the thermodynamics of bubbles at the collapse and rebound stage. Moreover, [88], studied the presence of the wall induces an asymmetric effect and a pressure gradient effect in the flow field around the bubble.

7.2 Numerical model and governing equations

This study employs a pure vapor bubble model, and its dynamics are assumed to be driven by inertia and compressible effects. The model assumes that the bubble is filled with compressible vapor, the condensable gas is neglected, and surrounding fluid is a static, compressible liquid. Flow is treated as laminar with no mass exchange between vapor and the flow field. The model also accounts for viscosity, thermodynamic effects,

and surface tension. Under the above assumptions, the liquid-vapor two-phase flow is treated as a homogeneous mixture by applying a volume of fluid (VOF) method. The density and momentum equation for the mixture is evaluated according to as discussed before in Chapter 2. The continuity equation reads as

$$\frac{\partial \rho_m}{\partial t} + \nabla \cdot (\rho \mathbf{u}) = 0 \tag{7.1}$$

The momentum equation for the homogeneous mixture is given by

$$\frac{\partial (\rho_m \mathbf{u})}{\partial t} + \nabla \cdot (\rho_m \mathbf{u}\mathbf{u}) = -\nabla p + \nabla \cdot \mu_m \nabla \mathbf{u} + \rho_m \mathbf{g} + \sigma \kappa \nabla \alpha \tag{7.2}$$

where ρ_m and μ_m are the density and viscosity of the mixture as defined earlier in equations (2.13) and (2.14) respectively. The surface tension coefficient is represented with the variable σ and κ is the curvature of interface, u the velocity vector, t is the time, p is the pressure, μ is the dynamic viscosity and g is the gravity. It can be noticed that heat and mass transfer are neglected. However, the additional transport equation for the temperature T is deduced from the energy equation

$$\frac{\partial (\rho_m T)}{\partial t} + \nabla \cdot (\rho_m \mathbf{u} T) = \nabla \cdot \mu_m \nabla T - (\frac{\alpha}{c_{\nu,w}} + \frac{1-\alpha}{c_{\nu,a}})(\frac{\partial \rho_m k}{\partial t} + \nabla \cdot (\rho_m \mathbf{u}) k + \nabla \cdot (\mathbf{u} p)) \tag{7.3}$$

with $k = \mathbf{u}^2/2$ the specific kinetic energy and $c_{v,a}$ and $c_{v,w}$ the specific heat capacities at constant volume for the air and water phases, respectively.

Moreover, the water volume fraction transport equation presents an additional source term due to the compressibility of the phase

$$\frac{\partial \alpha}{\partial t} + \nabla \cdot (\mathbf{u}\alpha) + \nabla \cdot (\mathbf{u_c} \alpha (1-\alpha)) = -\frac{\alpha}{\rho_w} \frac{D\rho_w}{Dt} \tag{7.4}$$

7.2.1 Geometry and parameters

In order to simulate the oscillation process of a spherical bubble near the horizontal rigid surface due to the pressure difference, we initialize a bubble of radius R_0 in a liquid cubic domain of dimensions $0.1 \times 0.1 \times 0.1$ m. For the representation of the bubble radius size and the distance to the wall, the normalized distance called a standoff distance γ is utilized

$$\gamma = \frac{L}{R_0} \tag{7.5}$$

where L is the distance between the initial bubble center and the wall, as shown in figure 7.1. The bottom boundary of the numerical domain is set as the rigid wall,

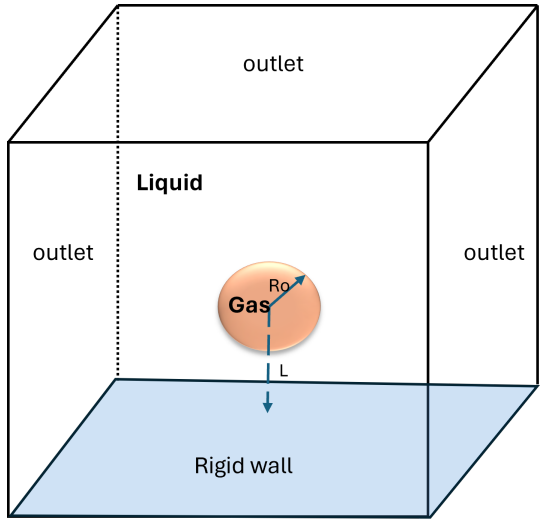

Figure 7.1: Schematic illustration of geometric model.

and the no-slip boundary condition is implemented. The rest of the surfaces are all defined as pressure outlets. The grid of $150 \times 150 \times 150$ mesh grid is adopted. The normalized distance γ is set as 1.2 by considering the initial radius $R_0 = 17.80$ mm and $L = 21.36$ mm. The initial pressure of the gas and liquid is set to 0.0031 MPa and 0.1013 MPa, respectively. The density of a gas is set to $1kg/m^3$, and liquid is set to $980kg/m^3$, and the initial temperature of both phases is set to be 300 K.

The numerical experiment is carried out in an OpenFoam and considering the *compressibleInterFoam* solver, which is an extension of the *interFoam* solver for two compressible non-isothermal and immiscible fluids using the Volume of Fluid, VOF. The boundary conditions for pressure outlets are implemented as non-reflected boundaries in order to save computational time. Hence, the "advective" outflow condition in the OpenFOAM toolbox is employed. The numerical simulation runs up to $5e^{-3}$s with the Courant number set to 0.25.

It is pertinent to mention here that we compared the bubble evolution in time with the experiment method by Huang et al. [89]. Later, this experiment was done numerically by [84]. Their results also match the well-known KK equation. Hence, in the present test case, the variation of the bubble radius is compared with the experimental solution and the RP equation. It is observed in figure 7.2 that the bubble evolution of the present test case and the experiment in the growth period is almost the same. In contrast, the bubble radius differs in the collapse and rebound stages. However, in comparison with the RP equation, the mismatch is caused by the assumption of the RP equation that the fluid is incompressible. The dimensionless

quantities radius R* and collapsing time t* used here are obtained from the Gua et al [90], defined as follows:

$$R* = \frac{R}{R_0} \tag{7.6}$$

$$t* = \frac{t}{t_0} \tag{7.7}$$

where

$$t_0 = R_0 \sqrt{\frac{\rho_{liquid}}{p_{liquid} - p_{gas}}} \tag{7.8}$$

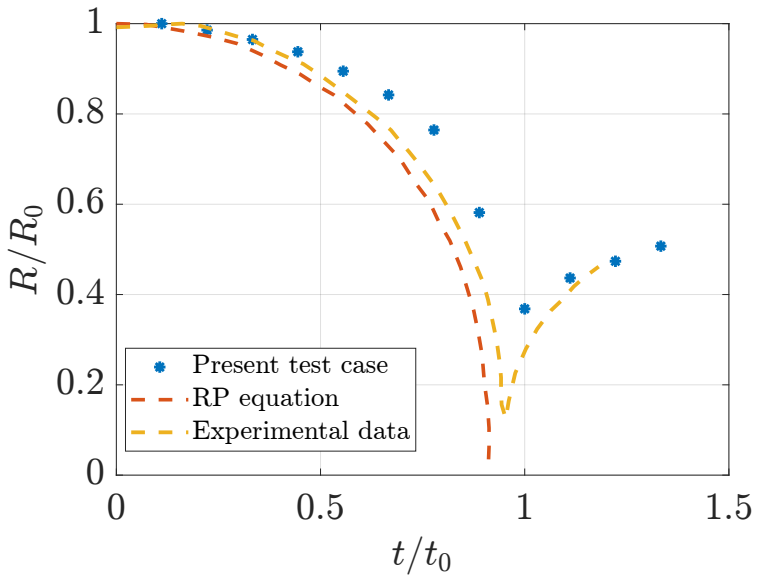

Figure 7.2: Comparison of the bubble radius evolution among present simulation, experimental data, and theoretical solution

7.2.2 Bubble evolution

The variation of bubble shapes in time with comparison to Huang experiment [89] are shown in figures (7.3). The variation is divided into two typical periods: the collapsing and rebounding periods. In the collapsing period, the volume of the bubble mainly performs contraction and "high-speed jet." For example, when t* = 0.0, the initial shape of the cavity near the rigid boundary is spherical. At t*=0.5, the bubble contracts, especially from the left and right sides of the bubble surface, leading to the bubble's ellipse-like shape. At t*=0.88, just before the collapsing time, the lower part of the bubble nearly reaches the rigid surface, and the rest of the bubble area shrinks

rapidly; hence, the speed at this stage of the bubble increases. Moreover, temperature also tends to be maximum at this period. When t* = 1.00, the bubble shape from the lower side turns to flat, while the lower side of the cavity has high pressure, resulting in the downward movement of the bubble as shown in figure (7.4a).

After that, at t*=1.1, the speed jet passes through the bubble and remains in an annular shape, which can be seen in figure (7.4b). At t*= 1.2, the rebound period of the bubble starts, and at t* = 1.8, the top of the bubble produces a "counter jet" as shown in figure (7.4c), which once again expands the volume of the bubble. The bottleneck-kind shape of the bubble is observed at t*=2.2. This numerical investigation of the bubble body has a satisfactory resemblance with the experimental results, apart from microbubbles caused by the rebound.

7.2.3 Quantitative analysis

In order to quantitatively investigate the relation between the flow structure and the thermodynamic parameters, we examine the maximum range of magnitude velocity, pressure, and temperature of the bubble at different times, In figure 7.5, it is observed that at the contraction stage of a bubble, the magnitude of the of velocity increases, the pressure decreases, and the temperature remains stable at $T = 300K$. At the collapse period at t*= 1.0, the magnitude of the velocity goes 20 m/s, and the maximum value of pressure $p = 0.8MPa$ is observed. This shows the formation of the "high-speed jet". Moreover, the bubble's maximum value of approximately 800 K is also seen. In the rebound period at t*= 2.0 the velocity begin to increase again, which exhibits the counter jet. Simultaneously, the the second peak of temperature of about $T = 370K$, showing the "counter jet". Later on, the pressure rebounds back, and a second peak of pressure is observed.

In general, we have observed the different stages of the single bubble by considering the thermal effects with the standoff distance γ =1.2. The high-speed and counter jets are observed. During the collapse period, we observed that the surface of the bubble rapidly contracted and produced significant heat. In the rebound stage, once again, the expansion of the volume of the bubble is observed due to the counter jet. The numerical results with the compressible two-phase solver are satisfactory, but to have more accurate results, a finer mesh will be considered, However, this introductory study primarily focused on a single bubble without varying the standoff distance. In the future, the bubble's hydrodynamic behavior and thermodynamic effect will be considered by varying the standoff distance. Moreover, we will investigate the interaction between bubbles close to a rigid surface, which is a crucial aspect of cavitation bubble analysis.

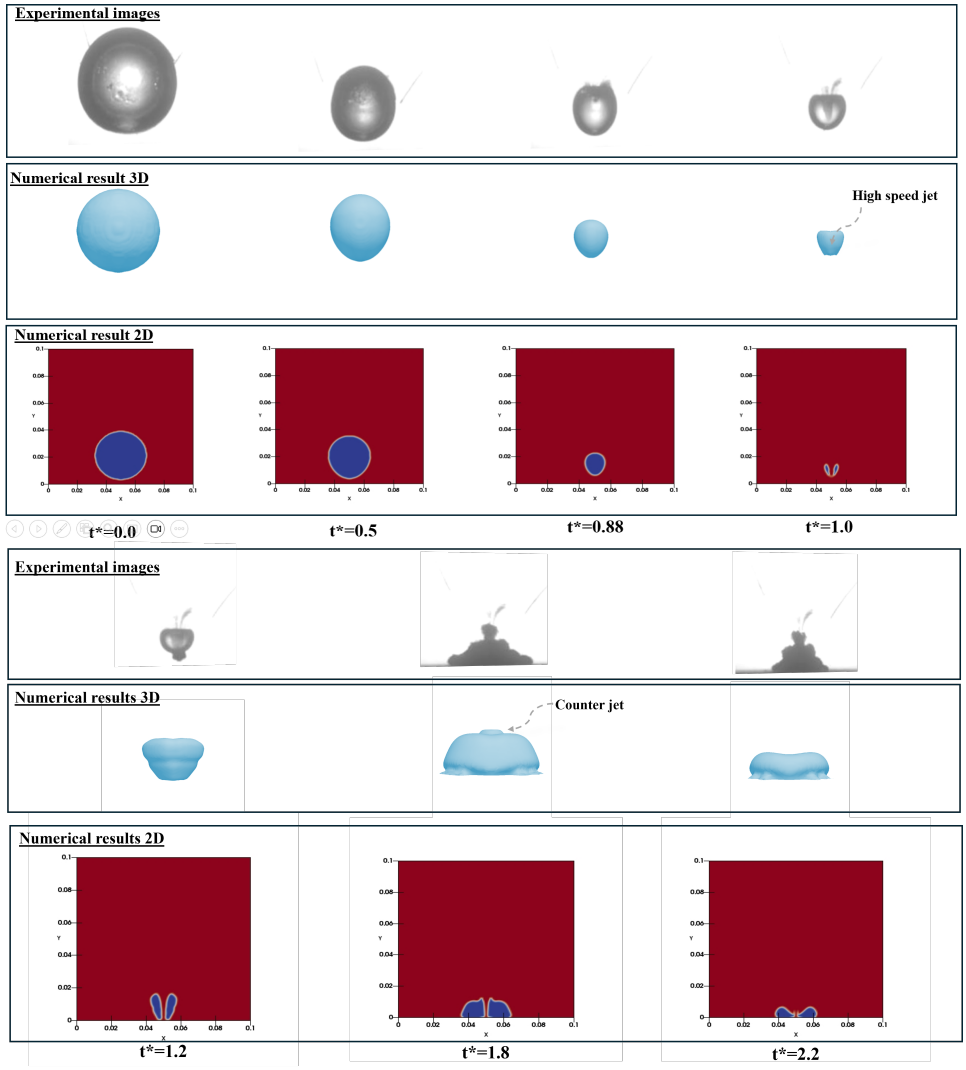

Figure 7.3: Comparison of the bubble shapes among experimental data ([89]), 3D and 2D numerical gas-liquid interface

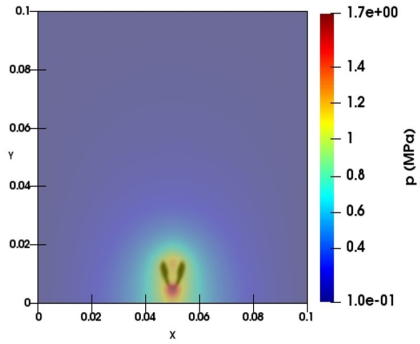

(a) High pressure at t*=1

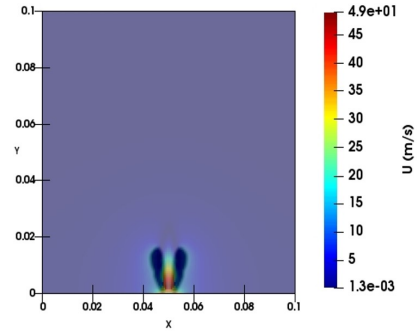

(b) High speed jet at t*=1.1

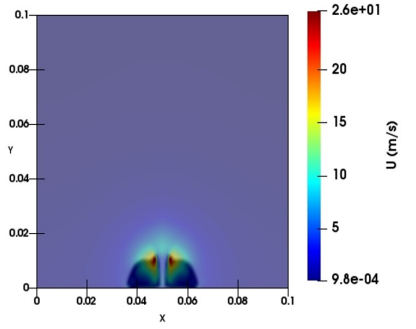

(c) Counter jet at t*=1.8

Figure 7.4: Evolution of bubble shapes showing highest pressure and speed jets

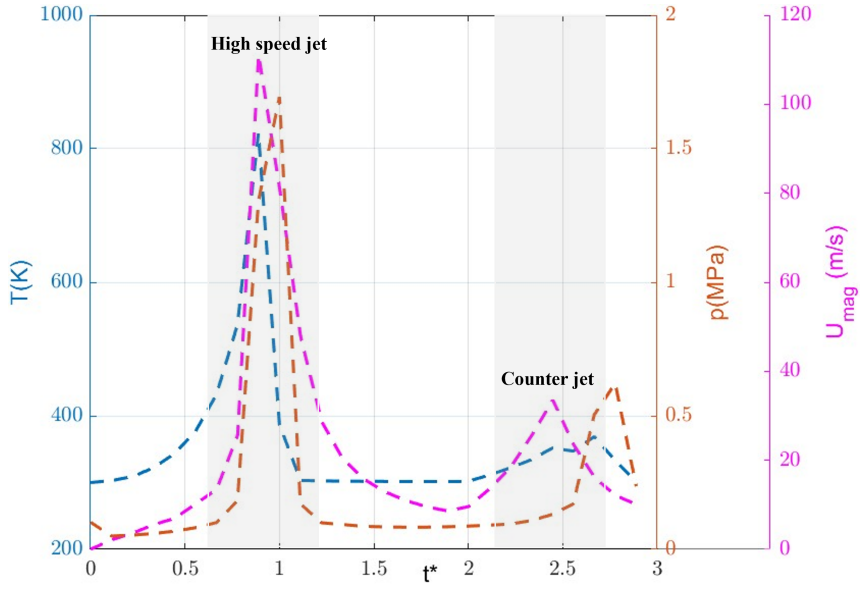

Figure 7.5: Comparison of velocity magnitude, temperature and pressure

Chapter 8

Conclusion

This dissertation is devoted to a unique area of acoustics, investigating the sound absorption property of a layer of air adhering to the wall plate in the presence of tonal acoustic waves in the low-to-intermediate frequency range ($\leq 1000\,\text{Hz}$). The use of an air bubble layer is a promising method to reduce the propagation of acoustic waves. Still, its applications have been limited to very high frequencies and isolated air mixtures. Our study, however, aimed to address a more realistic scenario.

The numerical experiments were conducted to reproduce a turbulent channel flow with an air inlet using a volume of fluid methodology to study the dynamics of the two-phase air-water flow. Two main cases of air layer were conducted, one with a low Reynolds number (LRN) with a longer domain and the other with a very high Reynolds number (HRN) with a narrow domain. In order to simulate the air layer in the turbulent flow, the first step was to set up a flow that would act as a precursor simulation for the inflow velocity field generation for the simulation with air introduced at the inlet. The simulation with LRN was simulated using Large Eddy Simulation (LES), with the air layer thickness 0.1 m close to the upper wall, and turbulent channel flow was considered a precursor simulation. However, for HRN, the simulation was conducted by considering a flat plate-like simulation using Wall-modeled Large Eddy Simulation (WMLES). Moreover, the layer simulated at HRN has been categorized into three cases. The first case involved a layer that started with pure air with thickness $\lambda_{a1} = 0.0022m$. The second case is with a layer that began with air with a thickness double of layer λ_{a1}, and the third case involves a layer that began with the mixed air with a thickness of λ_{a1}. These simulations aimed to obtain a realistic distribution of air, which was then used to define the properties of the acoustic domain, including density and speed of sound.

A numerical model based on the solution of the acoustic wave equation in the spatiotemporal domain was used to evaluate the propagation of a monopole source at different frequencies. The *hard source* method was employed for the implementation of source in the case of the layer with a low Reynolds number. Conversely, the soft

source method was utilized in the case of the air layer simulated with WMLES. The acoustic signal pressure is evaluated in SPL, and the difference between heterogeneous and homogeneous media is calculated. The average and instantaneous distribution of the air-water mixture layer was considered in the case of LRN. However, in the case of HRN, only the average field was taken into account. Moreover, in the propagation of acoustic waves in the case with HRN, the 3D model proved ineffective, especially in the case of mixed air at the inlet. Hence, the simpler 1D model was considered for the acoustic analysis.

In the case of the air layer with LRN, it was observed that the air mixture layer is more effective in blocking noise at higher frequencies, specifically at 1000 Hz. However, as the wavelength of the source increases, the effectiveness of the acoustic barrier diminishes for lower frequencies, such as 10 Hz. The study also found that the noise attenuation is more pronounced for the mean distribution of the air-water mixture layer compared to the instantaneous distribution.

In each case, the layer simulated at HRN, pure air with thickness λ_{a1} and doubling the thickness λ_{a1} and with mixed air, show a significant attenuation at 1000 Hz. However, the trend remains similar when varying the source signal frequency in the LRN layer, showing that the attenuation is less effective in lower frequencies.

Based on the comparisons, the air-water mixture layer with an average/even field proved more effective than an instantaneous air-water mixture distribution. Moreover, increasing the layer's thickness significantly enhances its efficacy in mitigating noise. Hence, for the optimal air barrier/curtain, it is recommended to prioritize a thicker and more uniform layer. Our further work will focus on studying the air-water layer's refinement under more realistic conditions and performing a 3D acoustic model more effectively. Additionally, we plan to explore the use of the Full Acoustic Analogy to introduce broadband continuous sources instead of monochromatic sources.

In engineering, air films are also utilized to minimize the destruction of water-submerged structures. Hence, the last part of the thesis was devoted to the cause of deterioration of underwater structures called cavitation erosion. The dynamics of cavitation are crucial to understanding because of the noise and material damage that can result from high velocities, pressures, and temperatures. The preliminary study concerning the dynamics of a single cavitation bubble collapse close to the rigid surface has been investigated. The process of collapsing the bubble with the evolution of temperature, pressure, and velocity field in time is investigated. The pure vapor bubble model is employed, and its dynamics are assumed to be driven by inertia and compressible effects. The two-phase CompressibleInterFoam solver in OpenFoam is utilized by considering the mixture model and applying the VoF approach. The collapse and rebound period of the bubble is observed with high-speed

jet moving in and out in proximity to the rigid wall. Moreover, the bubble contracted rapidly in the collapse stage, consequently exerting pressure on the vapor inside, leading to a significant temperature rise. The future study will include the variation of dimensionless standoff distance γ. Moreover, a finer mesh will be utilized to observe accurate results. The two-bubble interactions will also be considered near the rigid wall under the consideration of phase transitions as well as thermal effects.

Bibliography

[1] J. A. Hildebrand. Anthropogenic and natural sources of ambient noise in the ocean. *Marine Ecology Progress Series*, 395:5–20, 2009.

[2] A. O. MacGillivray, Z. Li, D. E. Hannay, K. B. Trounce, and O. M. Robinson. Slowing deep-sea commercial vessels reduces underwater radiated noise. *The Journal of the Acoustical Society of America*, 146(1):340–351, 2019.

[3] J. H. Spence and R. W. Fischer. Requirements for reducing underwater noise from ships. *IEEE Journal of Oceanic Engineering*, 42(2):388–398, 2016.

[4] A. J. Duncan, L. S. Weilgart, R. Leaper, M. Jasny, and S. Livermore. A modelling comparison between received sound levels produced by a marine vibroseis array and those from an airgun array for some typical seismic survey scenarios. *Marine pollution bulletin*, 119(1):277–288, 2017.

[5] M. Dahne, J. Tougaard, J. Carstensen, A. Rose, and J. Nabe-Nielsen. Bubble curtains attenuate noise from offshore wind farm construction and reduce temporary habitat loss for harbour porpoises. *Marine Ecology Progress Series*, 580:221–237, 2017.

[6] D. P. Loye and W. F. Arndt. A sheet of air bubbles as an acoustic screen for underwater noise. *The Journal of the Acoustical Society of America*, 20(2):143–145, 1948.

[7] B. Wursig, C. R. Greene Jr., and T. A. Jefferson. Development of an air bubble curtain to reduce underwater noise of percussive piling. *Marine environmental research*, 49(1):79–93, 2000.

[8] A. Tsouvalas and A. V. Metrikine. Noise reduction by the application of an air-bubble curtain in offshore pile driving. *Journal of Sound and Vibration*, 371:150–170, 2016.

[9] T. Bohne, T. Grießmann, and R. Rolfes. Modeling the noise mitigation of a bubble curtain. *The Journal of the Acoustical Society of America*, 146(4):2212–2223, 2019.

[10] Y. Peng, A. Tsouvalas, T. Stampoultzoglou, and A. Metrikine. Study of the sound escape with the use of an air bubble curtain in offshore pile driving. *Journal of Marine Science and Engineering*, 9(2):232, 2021.

[11] S. A. Mäkiharju, M. Perlin, and S. L. Ceccio. On the energy economics of air lubrication drag reduction. *International Journal of Naval Architecture and Ocean Engineering*, 4(4):412–422, 2012.

[12] Y. Murai. Frictional drag reduction by bubble injection. *Experiments in Fluids*, 55:1–28, 2014.

[13] D. Nagarathinam, K. Kim, B. Ahn, C. Park, G. Kim, and G. Yim. Experimental investigation of bubbly flow by air injection on an inclined hydrofoil. *Physics of Fluids*, 33(4), 2021.

[14] R.E. Arndt, C.R. Ellis, and S. Paul. Preliminary investigation of the use of air injection to mitigate cavitation erosion. *Journal of Fluids Engineering.*, 117(3):498–504, 1995.

[15] C. Wang, B. Huang, M.i Zhang, G. Wang, Q. Wu, and D. Kong. Effects of air injection on the characteristics of unsteady sheet/cloud cavitation shedding in the convergent-divergent channel. *International Journal of Multiphase Flow*, 106:1–20, 2018.

[16] A. J. C La Prairie. Method of blasting. 1955.

[17] L. M. Brekhovskikh and O. A. Godin. *Acoustics of Layered Media II: Point Sources and Bounded Beams*. Springer, 1992.

[18] O. A. Godin. Anomalous transparency of water-air interface for low-frequency sound. *Physical review letters*, 97(16):164301, 2006.

[19] O. A. Godin. Transmission of low-frequency sound through the water-to-air interface. *Acoustical Physics*, 53:305–312, 2007.

[20] O. A. Godin. Low-frequency sound transmission through a gas-liquid interface. *The Journal of the Acoustical Society of America*, 123(4):1866–1879, 2008.

[21] O. A. Godin. Sound transmission through water-air interfaces: New insights into an old problem. *Contemporary Physics*, 49(2):105–123, 2008.

[22] E. V. Glushkov, N. V. Glushkova, and O. A. Godin. The effect of anomalous transparency of the water-air interface for a volumetric sound source. *Acoustical Physics*, 59:6–15, 2013.

[23] D. C. Calvo, M. Nicholas, and G. J. Orris. Experimental verification of enhanced sound transmission from water to air at low frequencies. *The Journal of the Acoustical Society of America*, 134(5):3403–3408, 2013.

[24] B. E. McDonald and D. C. Calvo. Enhanced sound transmission from water to air at low frequencies. *The Journal of the Acoustical Society of America*, 122(6):3159–3161, 2007.

[25] E. E. Mikeska and I. A. Shooter. Sound pressure in air from a source in water for the case of a directional spherical wave. *The Journal of the Acoustical Society of America*, 69(S1):S61–S61, 1981.

[26] A. P. Voloshchenko and S. P. Tarasov. Effect of anomalous transparency of a liquid-gas interface for sound waves. *Acoustical physics*, 59:163–169, 2013.

[27] A. P. Voloshchenko and S. P. Tarasov. Experimental study of the transmission of low-frequency acoustic waves through a water–air interface. *The Journal of the Acoustical Society of America*, 145:143–148, 2019.

[28] P. Ghadimi, A. Bolghasi, M. A. Feizi Chekab, and R. Zamanian. Numerical investigation of transmission of low frequency sound through a smooth air-water interface. *Journal of Marine Science and Application*, 14:334–342, 2015.

[29] V. S. Shagapov and V. V. Sarapulova. Refraction and reflection of sound at the boundary of a bubbly liquid. *Acoustical Physics*, 61:37–44, 2015.

[30] D. A. Gubaidullin and Y. V. Fedorov. Acoustic wave incidence on a multilayer medium containing a bubbly fluid layer. *Fluid Dynamics*, 52(1):107–114, 2017.

[31] D. A. Gubaidullin and A. A. Nikiforov. Interaction of acoustic waves with bubbly layer with uneven distribution of bubbles. *Lobachevskii Journal of Mathematics*, 40:751–756, 2019.

[32] Y. Wang, D. Chen, X. Cao, and X. He. Theoretical and experimental studies of acoustic reflection of bubbly liquid in multilayer media. *Applied Sciences*, 12(23):12264, 2022.

[33] H. R. A. Mallock. The damping of sound by frothy liquids. *Proceedings of the Royal Society of London. Series A, Containing Papers of a Mathematical and Physical Character*, 84(572):391–395, 1910.

[34] A.B. Wood. *A Textbook of Sound*. MacMillan, 1930.

[35] D. Hsieh and M. S. Plesset. On the propagation of sound in a liquid containing gas bubbles. *The physics of fluids*, 4(8):970–975, 1961.

[36] K. W. Commander and A. Prosperetti. Linear pressure waves in bubbly liquids: Comparison between theory and experiments. *The Journal of the Acoustical Society of America*, 85(2):732–746, 1989.

[37] A. E. Ruggles, R. T. Lahey Jr, D. A. Drew, and H. A. Scarton. The relationship between standing waves, pressure pulse propagation, and critical flow rate in two-phase mixtures. *Journal of Mass and Heat Transfer*, 111(1):467–473, 1989.

[38] P. S. Wilson. Low-frequency dispersion in bubbly liquids. *Acoustics Research Letters Online*, 6(3):188–194, 2005.

[39] Preston S Wilson and Ronald A Roy. An audible demonstration of the speed of sound in bubbly liquids. *American Journal of Physics*, 76(10):975–981, 2008.

[40] G. Petris, M. Cianferra, and V. Armenio. Marine propeller noise propagation within bounded domains. *Ocean Engineering*, 265:112618, 2022.

[41] Christopher E Brennen. *Fundamentals of multiphase flow*. Cambridge university press, 2005.

[42] Amir Faghri and Yuwen Zhang. *Transport phenomena in multiphase systems*. Elsevier, 2006.

[43] Mamoru Ishii and Takashi Hibiki. *Thermo-fluid dynamics of two-phase flow*. Springer Science & Business Media, 2010.

[44] Martin Sommerfeld. *Modellierung und numerische Berechnung von Partikelbeladenen: turbulenten Strömungen mit Hilfe des Euler/Lagrange-Verfah*. Shaker, 1996.

[45] Kai Fu, Xiaolong Deng, Lingjie Jiang, and Pengfei Wang. Direct numerical study of speed of sound in dispersed air–water two-phase flow. *Wave Motion*, 98:102616, 2020.

[46] Cyril W Hirt and Billy D Nichols. Volume of fluid (vof) method for the dynamics of free boundaries. *Journal of computational physics*, 39(1):201–225, 1981.

[47] M. Cianferra and V. Armenio. Slowing deep-sea commercial vessels reduces underwater radiated noise. *Physics of Fluids*, xxx(x):xxx–xxx, 2024.

[48] Stephen B Pope. Turbulent flows. *Measurement Science and Technology*, 12(11):2020–2021, 2001.

[49] Osborne Reynolds. Iv. on the dynamical theory of incompressible viscous fluids and the determination of the criterion. *Philosophical transactions of the royal society of london.(a.)*, (186):123–164, 1895.

[50] J. Kim, P. Moin, and R. Moser. Turbulence statistics in fully developed channel flow at low reynolds number. *Journal of fluid mechanics*, 177:133–166, 1987.

[51] Joseph Smagorinsky. General circulation experiments with the primitive equations: I. the basic experiment. *Monthly weather review*, 91(3):99–164, 1963.

[52] U. Piomelli and E. Balaras. Wall-layer models for large-eddy simulations. *Annual review of fluid mechanics*, 34(1):349–374, 2002.

[53] Johan Larsson, Soshi Kawai, Julien Bodart, and Ivan Bermejo-Moreno. Large eddy simulation with modeled wall-stress: recent progress and future directions. *Mechanical Engineering Reviews*, 3(1):15–00418, 2016.

[54] Ugo Piomelli, Elias Balaras, Hugo Pasinato, Kyle D Squires, and Philippe R Spalart. The inner–outer layer interface in large-eddy simulations with wall-layer models. *International Journal of heat and fluid flow*, 24(4):538–550, 2003.

[55] Xiang IA Yang, George Ilhwan Park, and Parviz Moin. Log-layer mismatch and modeling of the fluctuating wall stress in wall-modeled large-eddy simulations. *Physical review fluids*, 2(10):104601, 2017.

[56] F. Nicoud and F. Ducros. Subgrid-scale stress modelling based on the square of the velocity gradient tensor. *Flow, turbulence and Combustion*, 62(3):183–200, 1999.

[57] Anthony Keating and Ugo Piomelli. A dynamic stochastic forcing method as a wall-layer model for large-eddy simulation. *Journal of Turbulence*, (7):N12, 2006.

[58] Ding Lee, George Botseas, and William L Siegmann. Examination of three-dimensional effects using a propagation model with azimuth-coupling capability (for3d). *The Journal of the Acoustical Society of America*, 91(6):3192–3202, 1992.

[59] A Tolstoy. 3-d propagation issues and models. *Journal of Computational Acoustics*, 4(03):243–271, 1996.

[60] Ying-Tsong Lin, Michael B Porter, Frédéric Sturm, Marcia J Isakson, and Ching-Sang Chiu. Introduction to the special issue on three-dimensional underwater acoustics. *The Journal of the Acoustical Society of America*, 146(3):1855–1857, 2019.

[61] Paul C Etter. Advanced applications for underwater acoustic modeling. *Advances in Acoustics and Vibration*, 2012, 2012.

[62] Allan D Pierce. *Acoustics: an introduction to its physical principles and applications*. Springer, 2019.

[63] M.E. Goldstein. *Aeroacoustics*. McGraw-Hill International Book Company, 1976.

[64] Giovanni Petris, Marta Cianferra, and Vincenzo Armenio. A numerical method for the solution of the three-dimensional acoustic wave equation in a marine environment considering complex sources. *Ocean Engineering*, 256:111459, 2022.

[65] Webe João Mansur, FS Loureiro, Delfim Soares Jr, and Cleberson Dors. Explicit time-domain approaches based on numerical green's functions computed by finite differences–the exga family. *Journal of Computational Physics*, 227(1):851–870, 2007.

[66] D Soares, WJ Mansur, and DL Lima. An explicit multi-level time-step algorithm to model the propagation of interacting acoustic-elastic waves using finite element/finite difference coupled procedures. *Computer Modeling in Engineering and Sciences*, 17(1):19, 2007.

[67] Dick Botteldooren. Finite-difference time-domain simulation of low-frequency room acoustic problems. *Journal of the Acoustical Society of America*, 98(6):3302–3308, 1995.

[68] Albert Chern. A reflectionless discrete perfectly matched layer. *Journal of Computational Physics*, 381:91–109, 2019.

[69] Stefan Bilbao and Brian Hamilton. Directional sources in wave-based acoustic simulation. *IEEE/ACM Transactions on Audio, Speech, and Language Processing*, 27(2):415–428, 2018.

[70] Jonathan Sheaffer, Maarten van Walstijn, and Bruno Fazenda. Physical and numerical constraints in source modeling for finite difference simulation of room acoustics. *The Journal of the Acoustical Society of America*, 135(1):251–261, 2014.

[71] Hyok Jeong and Yiu Wai Lam. Source implementation to eliminate low-frequency artifacts in finite difference time domain room acoustic simulation. *The Journal of the Acoustical Society of America*, 131(1):258–268, 2012.

[72] Michael Peter Norton and Denis G Karczub. *Fundamentals of noise and vibration analysis for engineers*. Cambridge university press, 2003.

[73] F. Lamonaca, G. Petris, M. Cianferra, and V. Armenio. Non-reflective hard source method for multiple physically extended sources and scattering bodies. *Physics of Fluids*, 36(3), 2024.

[74] F Ronald Young. *Cavitation*. World Scientific, 1999.

[75] Gert Kuiper. Cavitation research and ship propeller design. *Applied scientific research*, 58:33–50, 1997.

[76] Shengcai Li. *Cavitation of hydraulic machinery*, volume 1. World Scientific, 2000.

[77] Ezddin Hutli, Milos S Nedeljkovic, Nenad A Radovic, and Attila Bonyár. The relation between the high speed submerged cavitating jet behaviour and the cavitation erosion process. *International Journal of Multiphase Flow*, 83:27–38, 2016.

[78] Luca d'Agostino and Christopher E Brennen. Acoustical absorption and scattering cross sections of spherical bubble clouds. *The Journal of the Acoustical Society of America*, 84(6):2126–2134, 1988.

[79] William Henry Besant. *A treatise on hydrostatics and hydrodynamics*. Deighton, Bell, 1859.

[80] Lord Rayleigh. On the dynamics of revolving fluids. *Proceedings of the Royal Society of London. Series A, Containing Papers of a Mathematical and Physical Character*, 93(648):148–154, 1917.

[81] Milton S Plesset and Andrea Prosperetti. Bubble dynamics and cavitation. *Annual review of fluid mechanics*, 9(1):145–185, 1977.

[82] Joseph B Keller and Michael Miksis. Bubble oscillations of large amplitude. *The Journal of the Acoustical Society of America*, 68(2):628–633, 1980.

[83] H Yuan and Andrea Prosperetti. Gas-liquid heat transfer in a bubble collapsing near a wall. *Physics of Fluids*, 9(1):127–142, 1997.

[84] Zongyi Qin and Habib Alehossein. Heat transfer during cavitation bubble collapse. *Applied Thermal Engineering*, 105:1067–1075, 2016.

[85] Stacey L Meadley and Fernando A Escobedo. Thermodynamics and kinetics of bubble nucleation: Simulation methodology. *The Journal of chemical physics*, 137(7), 2012.

[86] S Schenke, Themistoklis Melissaris, and TJC Van Terwisga. On the relevance of kinematics for cavitation implosion loads. *Physics of Fluids*, 31(5), 2019.

[87] Qidong Yu, Xiaojian Ma, Zhicheng Xu, Jing Zhao, Dapeng Wang, and Zhenwei Huang. Thermodynamic effect of single bubble near a rigid wall. *Ultrasonics sonochemistry*, 71:105396, 2021.

[88] Bing Zhu, Wang Han, Wen-jun Xu, and Wei Zhang. Research on the collapse process of a near-wall bubble. *Journal of Hydrodynamics*, 35(5):899–912, 2023.

[89] Guohao Huang, Mindi Zhang, Xiaojian Ma, Qing Chang, Chen Zheng, and Biao Huang. Dynamic behavior of a single bubble between the free surface and rigid wall. *Ultrasonics sonochemistry*, 67:105147, 2020.

[90] Kaitao Guo, Di Zhao, and Lingxin Zhang. Theoretical research on the motion of spherical bubbles with surface tension. *Acta Mechanica Sinica*, 39(6):322341, 2023.